Influence of the Discretization Methods on the Distribution of Relaxation Times Deconvolution: Implementing Radial Basis Functions with DRTtools

Ting Hei Wan[a], Mattia Saccoccio[a], Chi Chen[a], Francesco Ciucci[a,b,*]

[a] *Department of Mechanical and Aerospace Engineering, The Hong Kong University of Science and Technology, Hong Kong, China*
[b] *Department of Chemical and Biomolecular Engineering, The Hong Kong University of Science and Technology, Hong Kong, China*

A B S T R A C T

The distribution of relaxation times (DRT) is an approach that can extract time characteristics of an electrochemical system from electrochemical impedance spectroscopy (EIS) measurements. Computing the DRT is difficult because it is an intrinsically ill-posed problem often requiring regularization. In order to improve the estimation of the DRT and to better control its error, a suitable discretization basis for the regularized regression needs to be chosen. However, this aspect has been invariably overlooked in the specialized literature. Pseudo-spectral methods using radial basis functions (RBFs) are, in principle, a better choice in comparison to other discretization basis, such as piecewise linear (PWL) functions, because they may achieve fast convergence. Furthermore, they can yield improved estimation by extending the estimated DRT to the entire frequency spectrum, if the underlying DRT decays to zero sufficiently fast outside the measured frequency range. Additionally, their implementation is relatively easier than other types of pseudo-spectral methods since they do not require *ad hoc* collocation point distributions. The as-developed novel RBF-based DRT framework was tested against controlled synthetic EIS spectra and real experimental data. Our results indicate that the RBF discretization performance is comparable with that of the PWL discretization at normal data collection range, and with improvement when the EIS acquisition is incomplete. In addition, we also show that applying RBF discretization for deconvolving the DRT problem can lead to faster numerical convergence rate as compared with that of PWL discretization only at error free situation. As a companion to this work we have developed a MATLAB GUI toolbox, which can be used to solve DRT regularization problems.

© 2015 Elsevier Ltd. All rights reserved.

1. Introduction

Due to its ability to provide useful information on both the reaction kinetics and transport phenomena, electrochemical impedance spectroscopy (EIS) [1] has been widely used to study complex electrochemical systems including lithium-ion batteries [2], fuel cells [3,4], ionic materials [5,6], solar cells [7,8], biological systems [9–11], and medical devices [12,13]. Extracting physico-chemical insights from the EIS is, however, non-trivial. Typically, EIS experiments are analyzed by fitting the impedance data against carefully chosen equivalent circuit models [14–17]. However, this method is sometimes limited because such equivalent circuits may not exist or multiple models may provide fits of analogous quality [1,18]. In this regard, the distribution of relaxation times (DRT) can

act as a useful alternative for interpreting EIS data [19] or to assist the equivalent circuit fitting based analysis [20].

The main goal of the DRT is to identify the characteristic distribution of typical EIS timescales. In order to do that, the experimental data Z_{exp} measured at given frequencies are "fitted" against a model Z_{DRT}, which is obtained from the following expression:

$$Z_{DRT}(f) = R_\infty + \int_0^\infty \frac{g(\tau)}{1 + i2\pi f\tau} d\tau \qquad (1)$$

where R_∞ is the ohmic resistance, and $g(\tau)$ is a suitable function that describes the time relaxation characteristics of the electro-chemical system studied. The expression (1) can be understood as an equivalent Voigt circuit. In other words, the DRT model impedance is composed by an Ohmic resistance (at $f \to \infty$) plus the sum of infinitely series of parallel resistors and capacitors. Since the frequency data is often collected on the logarithmic scale with a given number frequencies per decade, then (1) is

* Corresponding author. Tel.: +85297232394; fax: +85223581543.
E-mail address: francesco.ciucci@ust.hk (F. Ciucci).

Nomenclature

$\gamma(\tau)$	Distribution function of relaxation times, also written as $\gamma(\ln\tau)$
$\gamma_{\text{exact}}(\tau)$	Analytical solution of the DRT
$\hat{\gamma}(\tau)$	Deconvolved DRT
$\delta(\ln\tau)$	Dirac function centered at 0
$\phi_m(\tau)$	PWL discretization basis
$\phi_\mu(x)$	RBF discretization basis
Z_{DRT}	EIS for fitting the DRT model
Z_{exp}	Experimental EIS data
$\mathbf{Z}'_{\text{exp}}$	Real impedance vector
$\mathbf{Z}''_{\text{exp}}$	Imaginary impedance vector
$\mathbf{A}'$	Approximation matrix of the DRT for the real part of the EIS data
$\mathbf{A}''$	Approximation matrix of the DRT for the imaginary part of the EIS data
$\mathbf{M}$	Matrix of the norm of the first derivative of $\gamma(\tau)$
$\mathbf{L}$	Cholesky decomposition of M, i.e. $\mathbf{L}^T\mathbf{L} = \mathbf{M}$
$\mathbf{x}$	Vector of parameter for DRT approximation with respect to the discretization basis
$S(\mathbf{x})$	Sum of squares with respect to vector $\mathbf{x}$
R_∞	Ohmic resistance
R_{ct}	Charge transfer resistance
r^2	Residual
r^2_{tot}	Average total residual
r^2_{bias}	Average residual relative to bias
r^2_{var}	Average residual relative to variance
$v^2_{\text{bias}}(\tau)$	Integrand of the average residual relative to bias
$v^2_{\text{var}}(\tau)$	Integrand of the average residual relative to variance
f	Frequency
τ	Relaxation time
τ_0	Characteristic relaxation time
λ	Regularization parameter
μ	Shape factor of a RBF
ε	Error of the stochastic test

rewritten as:[1]

$$Z_{\text{DRT}} = R_\infty + \int_{-\infty}^{\infty} \frac{\gamma(\ln\tau)}{1 + i2\pi f\tau} d\ln\tau \qquad (2)$$

where $\gamma(\ln\tau) = \tau g(\tau)$

Finding $\gamma(\ln\tau)$ is challenging because fitting (2) against experimental data is an intrinsically ill-posed problem. Many methods for determining $\gamma(\ln\tau)$ have been developed and discussed in the literature, including the evolutionary programming techniques employed by Tsur and co-workers [22–25], Monte Carlo method as developed by Tuncer and McDonald [26,27], the maximum entropy method by Hörlin [28], and the Fourier filtering assisted fitting by Tiffée group and Boukamp [29,30]. In the present work we use the regularized regression approach [31–34]. The DRT is obtained by a two-step process: first, $\gamma(\ln\tau)$ is discretized in a convenient basis second, the discrete parameters are obtained by regularized regression.

The choice of the basis for discretizing $\gamma(\ln\tau)$ is of great importance because it can reduce the approximation error [35]. However, to our knowledge, the DRT literature still misses studies

focusing on the basis selection. Apart from the Voigt circuit approximation, the $\gamma(\ln\tau)$ can be estimated using piece-wise linear (PWL) approximation [36,37]. This approach assumes that the $\gamma(\ln\tau)$ is linear between each consecutive timescale studied. In this work, we focus on an alternative choice of basis, consisting of radial basis functions (RBFs), in order to enhance the DRT estimation quality.

RBFs have been widely utilized for approximating functions in applied mathematics [38,39], in areas as diverse as neural networks [40], partial differential equations [41], statistical estimation [42], machine learning [43], and computer graphics [44]. An RBF is a symmetric real-valued function depending on the distance from a given center, i.e., RBF $= \phi_\mu(|x - c|)$ where the center is located at $x = c$ and μ is a suitable scale factor or shape parameter. The major advantage of RBF-based approximations is their fast numerical convergence [38]. RBF-based approximations can achieve spectral accuracy, which means that the error of the approximation may decrease exponentially as the number of discretization points increases [45,46]. Moreover, RBF-based approximations can help to avoid any Runge phenomenon-like issues, that is, the problem of oscillation at the edges of an interval during high degree polynomial interpolation over a set of equispaced interpolation points [47]. Nonetheless, RBF-based approximation holds an extra advantage over other pseudo-spectra methods because it does not require any special distribution of the collocation points, which makes its implementation simpler and more flexible [47].

As described later in the article, applying RBF approximation has several important features. First, we are essentially generalizing the typical Voigt circuit approximation, which discretizes the DRT with a sum of Dirac distributions. Second, carefully chosen RBFs are defined over the entire frequency spectrum. Therefore, by applying RBFs to DRT estimation, we can extend the DRT interval from $\frac{1}{f_{\max}} \leq \tau \leq \frac{1}{f_{\min}}$ to the full set of relaxation times $0 \leq \tau < \infty$, when the underlying DRT decays to zero as $\tau \to 0$ and $\tau \to \infty$. Third, the shape factor can act as another regularizing parameter, in addition to the regularizing parameter with respect to the DRT derivative.

In this work, we developed RBF-based DRT, and we critically compared this approach with PWL-based DRT by applying both synthetic and real experiments. We show that the result of the RBF-based DRT is generally comparable with that of the PWL-based DRT at normal data collection range and improvement in convergence rate at error free situation. Moreover, as a result of extending the DRT results outside the measured frequency range with the RBF basis, the accuracy of the estimation improve only when the data collection frame is bounded by the experimental limitation. The code developed in this work is released as an open source MATLAB graphical user interface (GUI).

2. Theory

2.1. Discretization of the DRT

As outlined above, the Z_{DRT} is commonly approximated using Voigt circuits [48,49]. This approximation can be understood by writing $\gamma(\ln\tau)$ as a sum of Dirac distributions $\delta(\ln\tau)$ centered at M characteristic times $\tau_1, \tau_2, \ldots, \tau_M$, i.e.

$$\gamma(\ln\tau) = \sum_{m=1}^{M} x_m\delta(\ln\tau - \ln\tau_m) \qquad (3)$$

where x_m are unknown parameters to be estimated by fitting. Using the expression (3), the (2) may be simplified as [49,50]

$$Z_{\text{DRT}}(f) = R_\infty + \sum_{m=1}^{M} \frac{x_m}{1 + i2\pi f\tau_m} \qquad (4)$$

---

[1] This form of DRT model assumes that the inductive and capacitance feature of the data are insignificant. When inductive effect is not negligible, one should add $i\omega L$ into (2). When capacitive effect is significant, one should analyze the low frequency data in the effective capacitance plane [21].

Table 1
List of radial basis functions used in this work.

	$\phi_\mu(x)$	FWHM
Gaussian	$\exp\left(-(\mu x)^2\right)$	$\frac{1.665}{\mu}$
C2 Matérn	$\exp(-|\mu x|)(1 + |\mu x|)$	$\frac{3.357}{\mu}$
C4 Matérn	$\exp(-|\mu x|)\left(1 + |\mu x| + \frac{1}{3}|\mu x|^2\right)$	$\frac{4.661}{\mu}$
C6 Matérn	$\exp(-|\mu x|)\left(1 + |\mu x| + \frac{2}{5}|\mu x|^2 + \frac{1}{15}|\mu x|^3\right)$	$\frac{5.699}{\mu}$

Fitting the experimental data $Z_{\exp}(f_n)$ against $Z_{DRT}(f)$ is a well-posed problem if the number of Voigts element M is smaller than the number of experimental frequencies N [51]. Also, the DRT obtained will be discrete due to the nature of Dirac distributions. However, most electrochemical systems (e.g. the ZARC elements) are such that $\gamma(\ln\tau)$ is continuous. Therefore, one needs to approximate $\gamma(\ln\tau)$ as a sum of functions that are at least continuous. The use of PWL functions is perhaps the simplest approach. This consists of "tent" functions $\phi_1(\tau), \phi_2(\tau), ..., \phi_M(\tau)$ collocated at $\tau_1, \tau_2, ..., \tau_M$ respectively with the following expression [36,52]

$$\phi_m(\ln\tau) = \begin{cases} 1 - \dfrac{\ln\tau - \ln\tau_m}{\ln\tau_{m-1} - \ln\tau_m}, & \tau_{m-1} < \tau \le \tau_m \\ 1 - \dfrac{\ln\tau - \ln\tau_m}{\ln\tau_{m+1} - \ln\tau_m}, & \tau_m < \tau \le \tau_{m+1} \\ 0, & \tau < \tau_{m-1} \ \text{or} \ \tau > \tau_{m+1} \end{cases} \quad (5)$$

We then set the approximated $\gamma(\ln\tau)$ to be [37,53]

$$\gamma(\ln\tau) = \sum_{m=1}^{M} x_m \phi_m(\ln\tau) \quad (6)$$

where $\gamma(\ln\tau)$ is zero for $\tau < \tau_1$ and $\tau > \tau_M$ [36]. In order to extend the support of the approximated $\gamma(\ln\tau)$ to the set $-\infty < \ln\tau < \infty$, the Dirac distributions or the PWL functions may not be used. We need instead to use functions whose support extends to the entire real line. In this context, we can write that:

$$\gamma(\ln\tau) = \sum_{m=1}^{M} x_m \phi_\mu(|\ln\tau - \ln\tau_m|) \quad (7)$$

where $\phi_\mu(|\ln\tau - \ln\tau_m|)$ is an RBF with center timescale τ_m and shape parameter μ, see Table 1 for more details. The expansion (7) extends the Voigt circuits approximation, because it is physically equivalent to having M generalized RC circuits each characterized by a center characteristic timescale τ_m and a hierarchical distribution of infinitesimal RC circuits around that timescale as shown in Fig. 1. Various RBFs can be used for approximating the DRT. In this work we focus only on the special subset of positive-definite RBFs [54], namely Gaussian and differentiable Matérn functions up to order 6[2]. We choose the Matérn functions because their differentiability properties are not the same as those of Gaussians[3] (in contrast the PWL is differentiable only once). The RBFs used are summarized in Table 1.[4]

2.2. Estimation of the DRT

Upon discretizing $\gamma(\tau)$,[5] the DRT is estimated by fitting the impedance model $Z_{DRT}(f)$, described by (2), against the experimental data $Z_{\exp}(f)$. This can be obtained from a real EIS experiment or generated from a stochastic process. Fitting implies the minimization of the following sum of squares:

$$S = \sum_{n=1}^{N} \left[w'_n \left(Z'_{DRT}(f_n) - Z'_{\exp}(f_n)\right)^2 + w''_n \left(Z''_{DRT}(f_n) - Z''_{\exp}(f_n)\right)^2 \right] \quad (8)$$

If we set the impedance model $Z_{DRT}(f_n)$, given in equation (1), in matrix form as:

$$Z_{DRT}(f_n) = R_\infty + (\boldsymbol{A}'\boldsymbol{x})_n + (\boldsymbol{A}''\boldsymbol{x})_n \quad (9)$$

where the matrixes A' and A'' can be found in the Appendix, then we can rewrite (8) as:

$$S(\boldsymbol{x}) = \left\| \boldsymbol{\Omega}' \left(R_\infty \boldsymbol{1} + \boldsymbol{A}'\boldsymbol{x} - \boldsymbol{Z}'_{\exp} \right) \right\|^2 + \left\| \boldsymbol{\Omega}'' \left(\boldsymbol{A}''\boldsymbol{x} - \boldsymbol{Z}''_{\exp} \right) \right\|^2 \quad (10)$$

where $\boldsymbol{1}$ is a column vector with N entries all equal to 1. The expression of $\boldsymbol{\Omega}'$ and $\boldsymbol{\Omega}''$ can be found in the Appendix. By minimizing $S(\boldsymbol{x})$, one can obtain the vector $\boldsymbol{x}$, which can then be applied to estimate $\gamma(\tau)$ using relation (7), as illustrated in Fig. 2. However, as previously mentioned, the problem above is ill-posed if $M \approx N$ or $M >> N$ [51]. That is, minimizing $S(\boldsymbol{x})$ will likely result in an oscillating DRT. The reduction of these oscillations can be achieved by adding an extra penalty, which can be a term proportional to the norm of the first or second derivative of the $\gamma(\tau)$ function, i.e., $\left\| s\dfrac{d\gamma(\tau)}{d\ln\tau}s \right\|^2$. If this term is added to (10), then $S(\boldsymbol{x})$ can be then rewritten as:

$$S(\boldsymbol{x}) = \left\| \boldsymbol{\Omega}' \left(R_\infty \boldsymbol{1} + \boldsymbol{A}'\boldsymbol{x} - \boldsymbol{Z}'_{\exp} \right) \right\|^2 + \left\| \boldsymbol{\Omega}'' \left(\boldsymbol{A}''\boldsymbol{x} - \boldsymbol{Z}''_{\exp} \right) \right\|^2 + \lambda \boldsymbol{x}^T \boldsymbol{M} \boldsymbol{x} \quad (11)$$

where the matrix $\boldsymbol{M}$ is derived in Appendix A. The minimization of $S(\boldsymbol{x})$ is the well-known Tikhonov regularization problem. We can apply Cholesky decomposition of $\boldsymbol{M}$, i.e., $\boldsymbol{M} = \boldsymbol{L}^T\boldsymbol{L}$, where $\boldsymbol{L}$ is a lower triangular matrix with real and positive diagonal entries [55]. Therefore, (11) can be rewritten as:

$$S(\boldsymbol{x}) = \left\| \boldsymbol{\Omega}' \left(R_\infty \boldsymbol{1} + \boldsymbol{A}'\boldsymbol{x} - \boldsymbol{Z}'_{\exp} \right) \right\|^2 + \left\| \boldsymbol{\Omega}'' \left(\boldsymbol{A}''\boldsymbol{x} - \boldsymbol{Z}''_{\exp} \right) \right\|^2 + \lambda \left\| \boldsymbol{L}\boldsymbol{x} \right\|^2 \quad (12)$$

Minimizing $S(\boldsymbol{x})$ ensures that the DRT result adheres well to the data with the oscillations controlled by the coefficient λ. The greater the λ, the lesser the DRT osciμllation. The λ value, however, cannot be too large as it may cause over smoothing, resulting in the loss of features that carry physically relevant information. To compare the various discretization methods, we choose λ such that the squared residual between numerically computed DRT and the exact DRT is minimized. As a supplement, we apply Re-Im cross validation [36] to estimate the optimal λ.

We note that $\boldsymbol{A}'$ and $\boldsymbol{A}''$ in (11) highly depend on the shape factor of the RBF μ. As shown in Table 1 μ is related to the full width at half maximum (FWHM) of the RBFs used for discretization. The smaller μ is, the greater will be the FWHM of the RBFs as indicated

---

[2] The PWL function is a symmetric real-valued function depending on the distance from the collocation center when the collocation points are evenly distributed. In other word, a PWL function can be regarded as a RBF when it is applied to uniform collocation points.

[3] The C2 Matérn is twice differentiable, the C4 Matérn is 4 times differentiable, and the C6 Matérn is 6 times differentiable, while the Gaussian RBF is differentiable infinitely many times.

[4] The MATLAB GUI developed in this study can also deal with other types of RBF, including inverse quadric, inverse quadratic, and Cauchy functions.

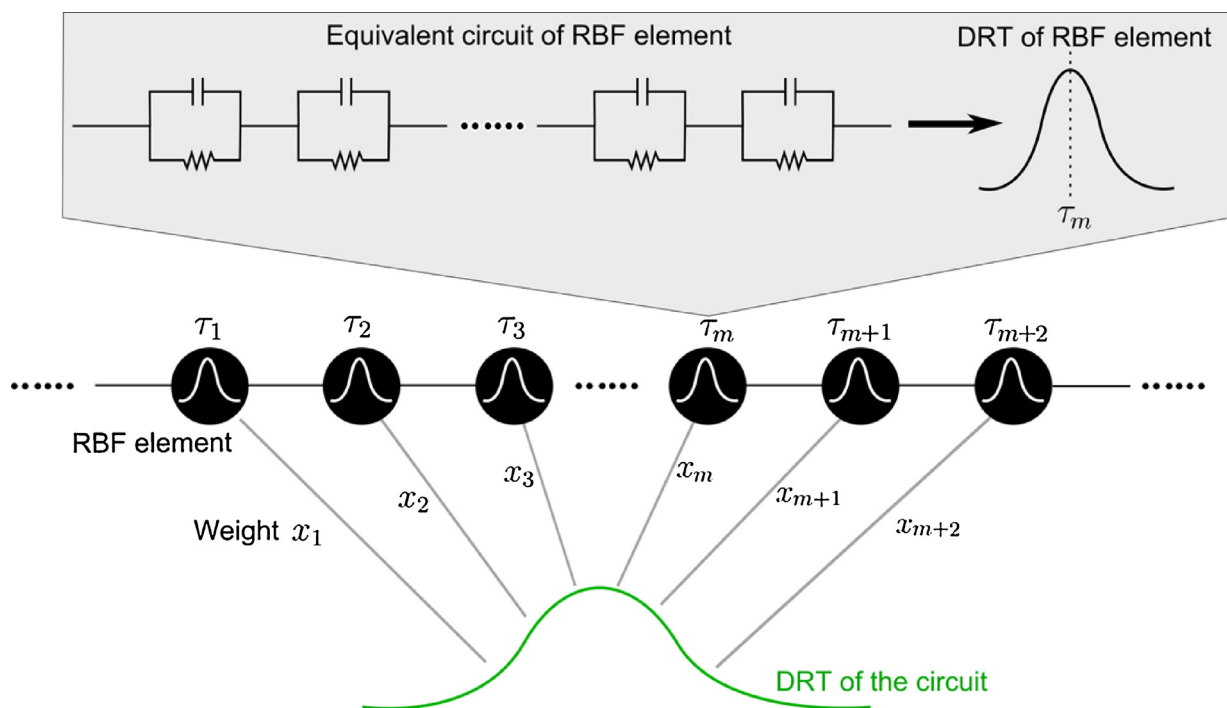[5] With some abuse of notation, we identify $\gamma(\ln\tau)$ with $\gamma(\tau)$.
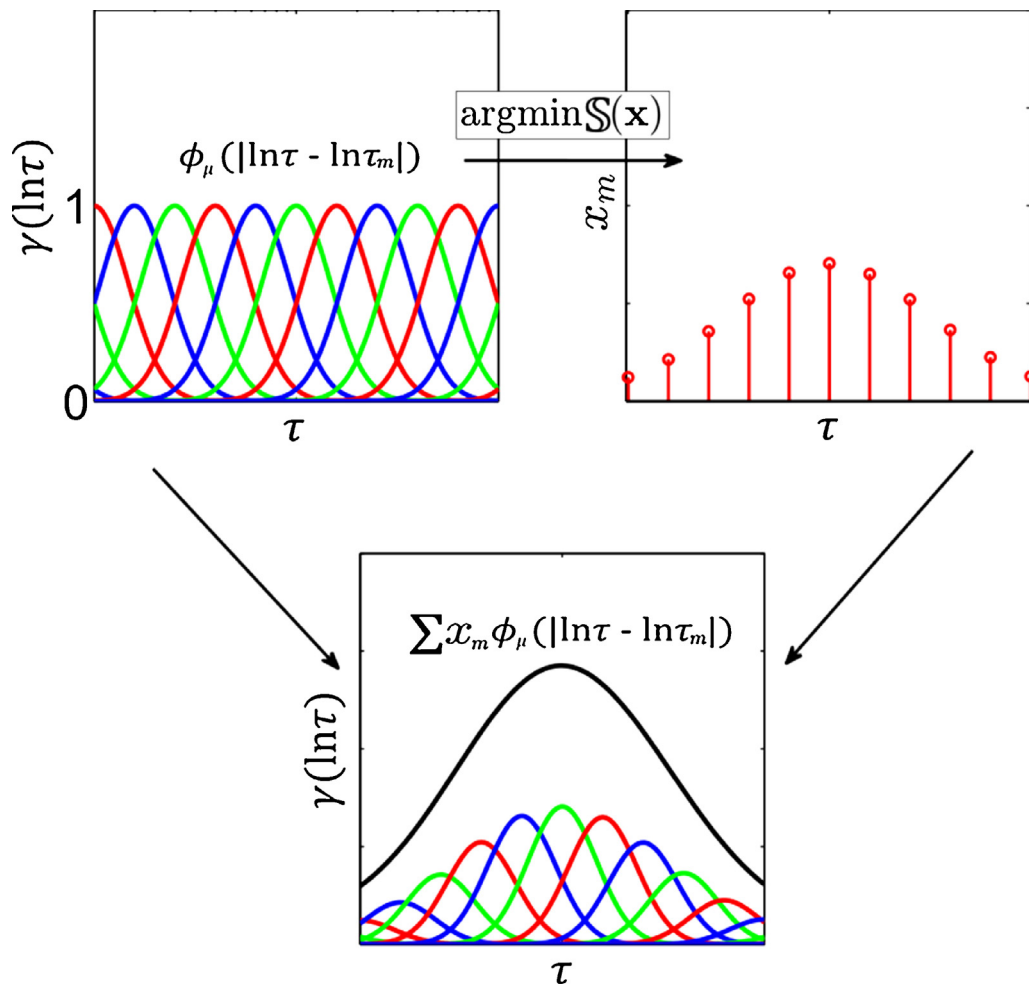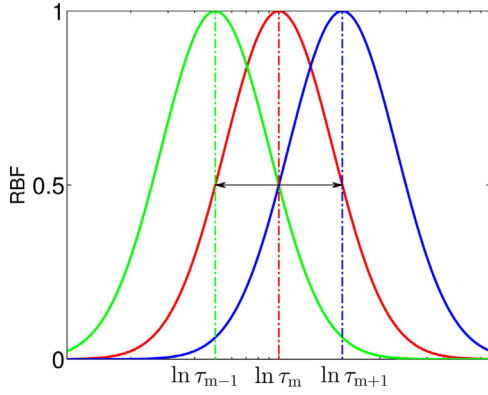
Fig. 1. Schematic of the DRT using RBF discretization.

Fig. 2. Schematic of the RBF–based DRT. $\gamma(\tau)$ is first discretized with RBFs as a function of vector of parameters $\boldsymbol{x}$ (top left panel). Minimizing the sum of squares leads to estimation of $\boldsymbol{x}$ (top right panel). $\gamma(\ln\tau)$ is estimated from $\boldsymbol{x}$ (bottom panel).

Fig. 3. Schematic showing the relation between the FWHM and the separation of the collocation points applied in this study. The double arrow indicates the FWHM for the central RBF.

Fig. 4. The bias-variance tradeoff of the computed DRT of the ZARC model using Gaussian discretization. The vertical green dash-dot line indicates the value of the regularization parameter λ, which minimized the total residual.

by the double arrow of Fig. 3. In general, if μ is large, the computed DRT will be endowed with a discrete nature, and it will oscillate near each collocation point[6]. On the other hand, if μ is small, the computed DRT may be flattened, leading to the disappearance of local DRT features. This implies that the shape factor μ is another potential regularizing tool for the DRT analysis. Here, we choose μ such that FWHM of the RBFs used for discretization is equal to twice the distance between two consecutive collocation points. Under the assumption that the collocation points are equally spaced in logarithm scale, we can write that:

$$\text{FWHM} = 2(\Delta\ln\tau) \tag{13}$$

Using the relation (13), the FWHM of the RBFs at collocation point τ_m equals the log-scale distance between τ_{m-1} and τ_{m+1}, as illustrated in Fig. 3.

2.3. Stochastic Experiments

We will employ stochastic experiments obtained from EIS spectra with close form DRT to demonstrate the applicability of the RBFs for DRT approximation. The synthetic experiments data $Z_{exp}(f)$ are obtained from a noise-corrupted analytical model $Z(f)$ [56]:

$$Z_{exp}(f) = Z(f) + \varepsilon|Z(f)|(\eta' + i\eta'') \tag{14}$$

where ε is the noise level (we take $\varepsilon = 0.5\,\%$ in following study unless otherwise specified), and η' and η'' are two independent normally distributed random variables with 0 mean and unit variance. While the proposed error structure is plausible and corresponds to a weight proportional to the absolute value of the impedance, the errors may take a more complicated form depending on the particular system studied as discussed by other authors [18,57]. In order to generalize this work, we will also analyze with DRT the impedance spectroscopy data obtained from real experiments.

2.4. Benchmarking the Computed DRT

In order to compare the quality of the proposed approximations, we will use the normalized relative squared residual r^2 defined as the square of the difference between the estimated DRT,
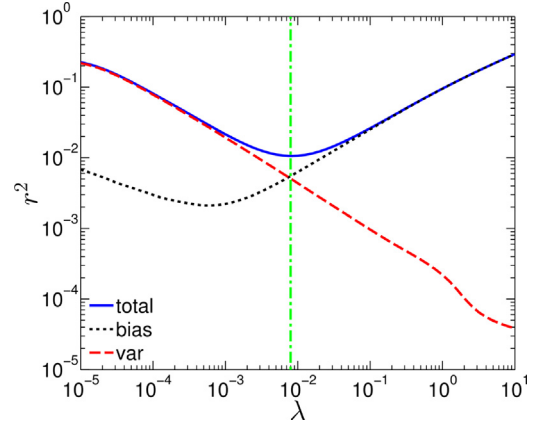
$\hat{\gamma}(\tau)$, and the analytical (also the exact) DRT, $\gamma_{exact}(\tau)$, divided by the square of the norm of the exact DRT, that is:

$$r^2 = \frac{\int_{-\infty}^{\infty}(\gamma_{exact} - \hat{\gamma})^2 d\ln\tau}{\int_{-\infty}^{\infty}\gamma_{exact}^2 d\ln\tau} \tag{15}$$

where, for brevity, we omit the τ argument in the right hand side. The average squared residual obtained from a batch of K synthetic experiments is given by:

$$r_{tot}^2 = \frac{1}{K}\sum_{k=1}^{K}\frac{\int_{-\infty}^{\infty}(\gamma_{exact} - \hat{\gamma}_k)^2 d\ln\tau}{\int_{-\infty}^{\infty}\gamma_{exact}^2 d\ln\tau} \tag{16}$$

where the subscript k denotes the DRT estimated from the kth simulated experiment. In fact, r_{tot}^2 can be regarded as the sum of two squared residual, the first squared residual is the bias while the second is the variance[7]:

$$r_{tot}^2 = r_{bias}^2 + r_{var}^2 \tag{17}$$

where

$$r_{bias}^2 = \frac{\int_{-\infty}^{\infty}\left(\gamma_{exact} - \frac{1}{K}\sum_{j=1}^{K}\hat{\gamma}_j\right)^2 d\ln\tau}{\int_{-\infty}^{\infty}\gamma_{exact}^2 d\ln\tau} \tag{18}$$

and

$$r_{var}^2 = \frac{1}{K}\sum_{k=1}^{K}\frac{\int_{-\infty}^{\infty}\left(\hat{\gamma}_k - \frac{1}{K}\sum_{j=1}^{K}\hat{\gamma}_j\right)^2 d\ln\tau}{\int_{-\infty}^{\infty}\gamma_{exact}^2 d\ln\tau} \tag{19}$$

With these indicators, we will compare the different discretization methods by monitoring r_{tot}^2. To investigate how the bias and variance depend on τ, we shall also define the following two quantities:

$$v_{bias}^2(\tau) = \frac{\left(\gamma_{exact}(\tau) - \frac{1}{K}\sum_{j=1}^{K}\hat{\gamma}_j(\tau)\right)^2}{\int_{-\infty}^{\infty}\gamma_{exact}^2 d\ln\tau}$$

---

[6] When the area normalized Gaussian RBF $\phi_\mu(x) = \frac{\mu}{\sqrt{\pi}}\exp\left(-(\mu x)^2\right)$ is used for discretization and if $\mu \to \infty$ then the Voigt, (3), and the RBF representation, by (7), coincide. In such a case, RBF can also be applied to solve for discrete $\gamma(\ln\tau)$, e.g. models consist of RC elements.

[7] The relationship of (17) to (19) can be verified by noticing that,

Table 2
The minimum residual, optimal λ, and predicted optimal λ from cross validation test for the ZARC model with different discretization functions and data collection scenarios.

	Normal range 10 ppd			Normal range 5 ppd			Half width range 10 ppd		
	r_{tot}^2	λ_{OPT}	λ_{CV}	r_{tot}^2	λ_{OPT}	λ_{CV}	r_{tot}^2	λ_{OPT}	λ_{CV}
Piecewise linear	1.07E-02	1.91E-03	2.14E-03	1.52E-02	2.63E-03	2.88E-03	1.61E-02	2.75E-03	3.09E-03
Gaussian	1.05E-02	8.13E-03	7.41E-03	1.38E-02	5.89E-03	5.89E-03	1.15E-02	6.76E-03	9.55E-03
C2 Matérn	9.93E-03	7.94E-03	7.94E-03	1.31E-02	5.01E-03	6.46E-03	1.18E-02	6.31E-03	1.02E-02
C4 Matérn	9.61E-03	8.91E-04	8.32E-04	1.40E-02	6.31E-04	6.31E-04	1.14E-02	7.59E-04	1.07E-03
C6 Matérn	1.02E-02	3.80E-05	3.72E-05	1.35E-02	2.63E-05	3.39E-05	1.19E-02	2.88E-05	4.47E-05
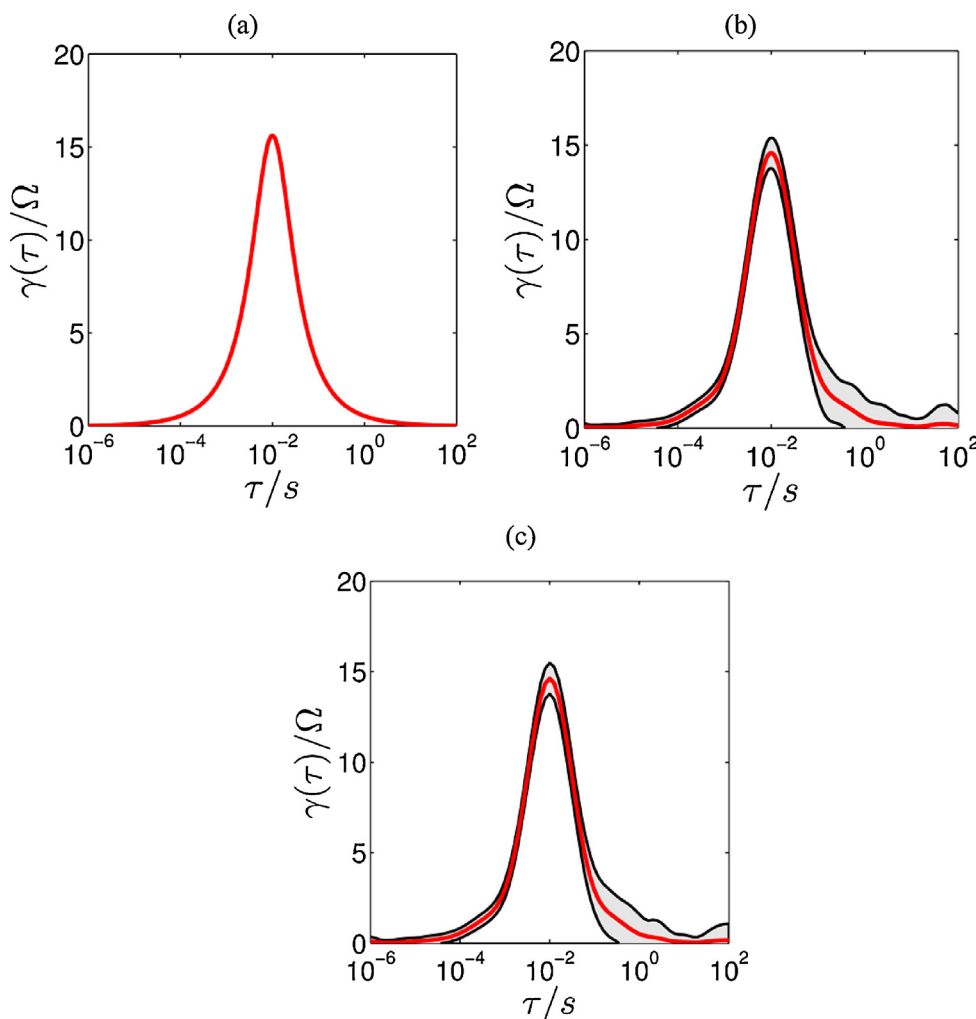
Fig. 5. The exact DRT result of the ZARC element case, panel (a), the average computed DRT with normal data range and 10 ppd data collection density using Gaussian discretization, panel (b), and using PWL discretization, panel (c), at optimal λ. The grey band in panel (b) and (c) shows the 3σ confidence interval of the result.

and

$$v_{var}^2(\tau) = \frac{1}{K}\sum_{k=1}^{K}\frac{\left(\hat{\gamma}_k(\tau) - \frac{1}{K}\sum_{j=1}^{K}\hat{\gamma}_j(\tau)\right)^2}{\int_{-\infty}^{\infty}\gamma_{exact}^2 d\ln\tau} \quad (21)$$

where $r_{bias}^2 = \int_{-\infty}^{\infty} v_{bias}^2(\tau)d\ln\tau$ and $r_{var}^2 = \int_{-\infty}^{\infty} v_{var}^2(\tau)d\ln\tau$.

3. Results and Discussion

We tested the performance of the RBF discretization using both synthetic and real experiments. In the first part, we used different discretizations, based on RBFs and PWL functions, and benchmarked the DRT quality obtained from synthetic EIS experiments. Synthetic experiments are needed since the inverse problem of approximating for the DRT is susceptible to the noise of the data. In the second part, we applied the RBF-based DRT to a battery example.

These synthetic experiments were based on three simple models: a ZARC element [58], two ZARCs in series [59], and a Havriliak-Negami element [60]. The availability of closed form analytical solutions from literature for the three chosen models allows comparison with the computed results[8]. To illustrate the advantage of applying RBFs, we considered three data collection scenarios: 1)

---

[8] The analytical solution of an impedance model can be derived by the equation $\gamma(\tau) = -\frac{1}{\pi}\left[Z'\left(e^{-\ln\tau + \frac{i\pi}{2}}\right) + Z''\left(e^{-\ln\tau - \frac{i\pi}{2}}\right)\right]$ [61].
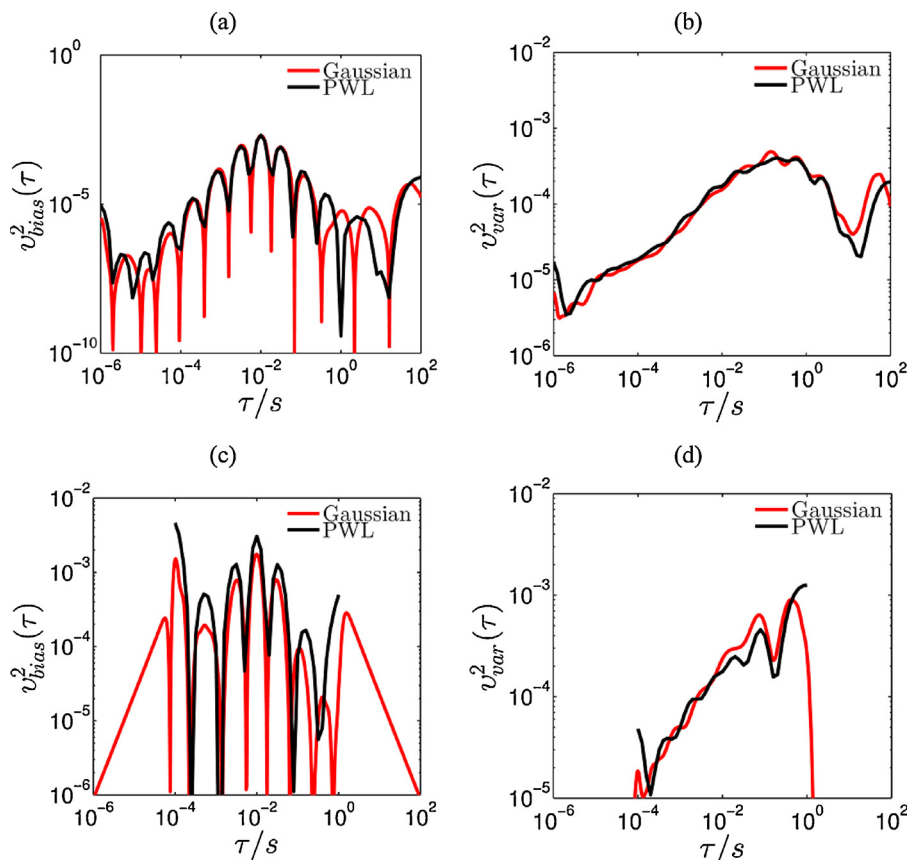
Fig. 6. The residual due to bias, panel (a), (c), and residual due to variance, panel (b), (d), over the range of ZARC case at λ_{OPT}. Panel (a) and (b) are the residual results for the normal data range 10 ppd. Panel (c) and (d) are the residual results for the reduced data range.

normal range (10^{-2} Hz $< f_m < 10^6$ Hz) with 10 ppd (collocation points per decade), 2) normal range with 5 ppd and 3) half range (10^0 Hz $< f_m < 10^4$ Hz) with 10 ppd. We firstly demonstrated that regularization with RBF discretization can actually lead to a reasonable approximation of the exact DRT of various models. As the EIS data point distribution is an important factor affecting the DRT approximation quality, we then studied the effect of collocation points density and data collection range on the approximated DRT. This, in turn, allowed us to investigate how the performance of the RBF-based DRT compared with PWL-based DRT under different scenarios.

### 3.1. Synthetic Experiments

3.1.1. ZARC Model

Firstly, we took synthetic experiments obtained from an exact ZARC model. We considered this case because it is commonly used when interpreting the EIS of practical systems including fuel cells and batteries [62,63]. The ZARC model is basically a resistor (R_∞) in series with a circuit comprising a constant phase element (CPE) in parallel with a resistor [58]. The impedance response of this ZARC model is given by:

$$Z(f) = R_\infty + \frac{R_{ct}}{1 + (i2\pi f \tau_0)^\phi} \tag{22}$$

where $R_\infty = 10\ \Omega$, $R_{ct} = 50\ \Omega$, $\tau_0 = 0.01$ s and $\phi = 0.7$. The corresponding $\gamma(\tau)$ is given by [19]

$$\gamma(\tau) = \frac{R_{ct}}{2\pi} \frac{\sin((1-\phi)\pi)}{\cosh\left(\phi \ln\left(\frac{\tau}{\tau_0}\right)\right) - \cos((1-\phi)\pi)} \tag{23}$$

After randomly drawing 1000 synthetic experiments, we performed regularized regression at various λ. As shown in Fig. 4, for the case of Gaussian discretization the r_{tot}^2 strongly depends on the regularization parameter λ, where the squared residual variance r_{var}^2 dominates at low λ values and the squared residual bias r_{bias}^2 dominates at high λ values. This is intuitive because the smaller the value of λ, the larger the oscillations are. This implies that the computed DRT has large variance. On the other hand, the larger the value of λ, the greater the flattening effect of the regularization term. Therefore, there will be greater mismatch between the exact DRT and estimated DRT. The average squared residuals for other types of discretizations can also be plotted with respect to λ that gives a similar trend. Thus, we can obtain the optimal λ, denoted as λ_{OPT}, for each type of discretization and each data collection scenario. We stress that for λ_{OPT} the combined effect of the squared residuals relative to the variance and the squared residuals relative to bias is minimized. For comparison, the predicted optimal λ values, denoted as λ_{CV}, are also obtained through the Re-Im cross-validation tests. Table 2 shows the λ_{OPT} values, the λ_{CV} values and the average squared residuals of the computed DRT at λ_{OPT} for different discretization methods. As illustrated in Fig. 5, at λ_{OPT} the average DRT as computed using the PWL (panel c) and Gaussian function (panel b) are reasonably close to the exact solution shown in Fig. 5a. This is reflected also by the average squared residual as shown in Table 2. Because of the synthetic error, the as-computed DRTs from individual sets of stochastic data are not identical to one another. We have calculated the relaxation time dependent variance σ of the computed results over τ. The 3σ confidence band is indicated by the grey region as shown in Fig. 5. We also notice that in Table 2 the average squared residuals of the four
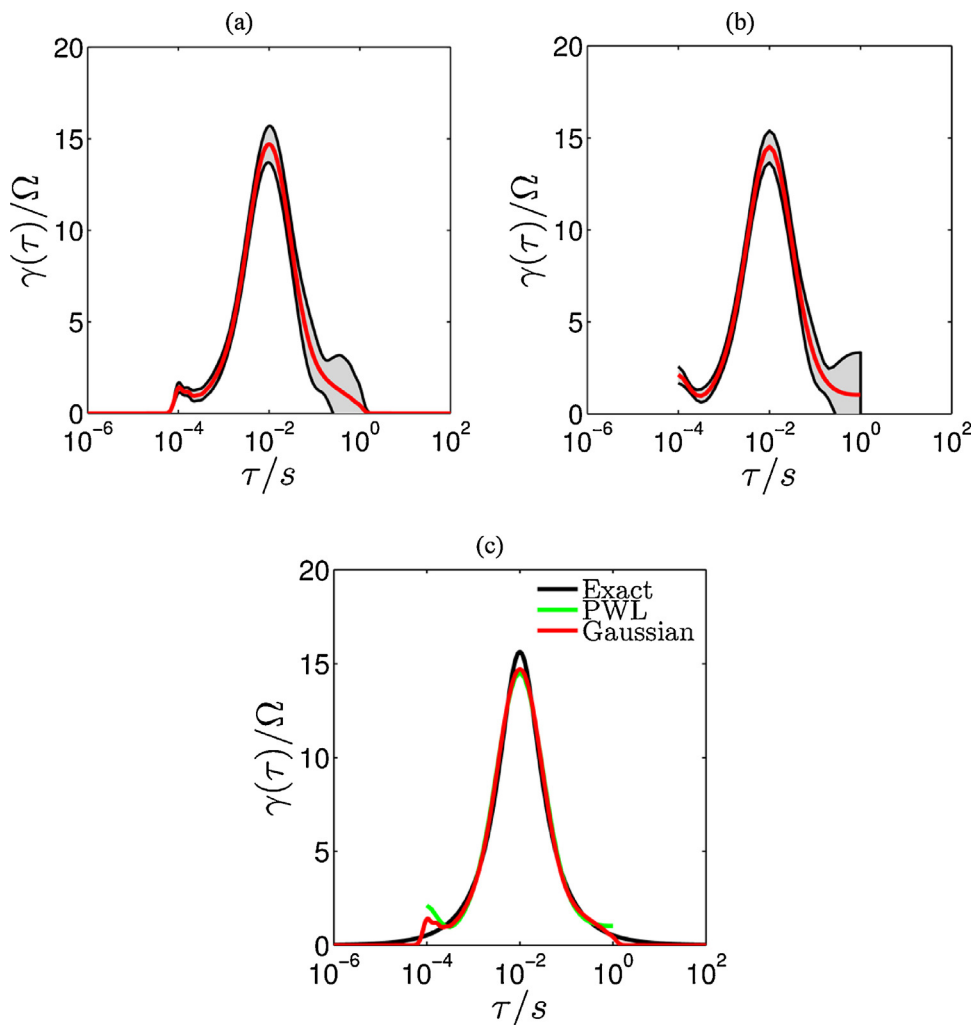
Fig. 7. The average DRT value and the confidence region for Gaussian discretization, panel (a) and PWL discretization, panel (b) for the ZARC case with half data collection width. Panel (c) shows the comparison of the average values with the exact solution.

types of RBF discretization are similar for all of the data collection scenarios. This can be attributed to the fact that we set μ of each RBF based on relation (13) keeping identical FWHMs for all RBFs. Thus, in order to streamline the following discussion, we shall use Gaussian function as the representative RBF.
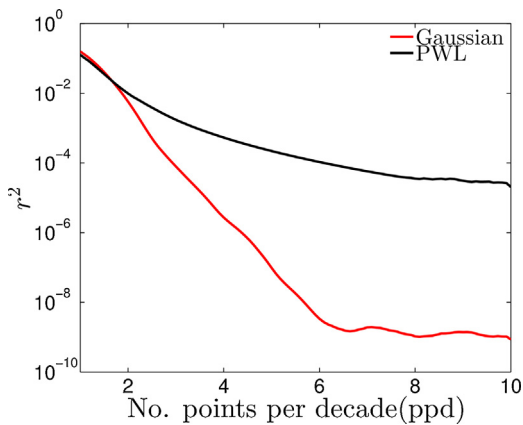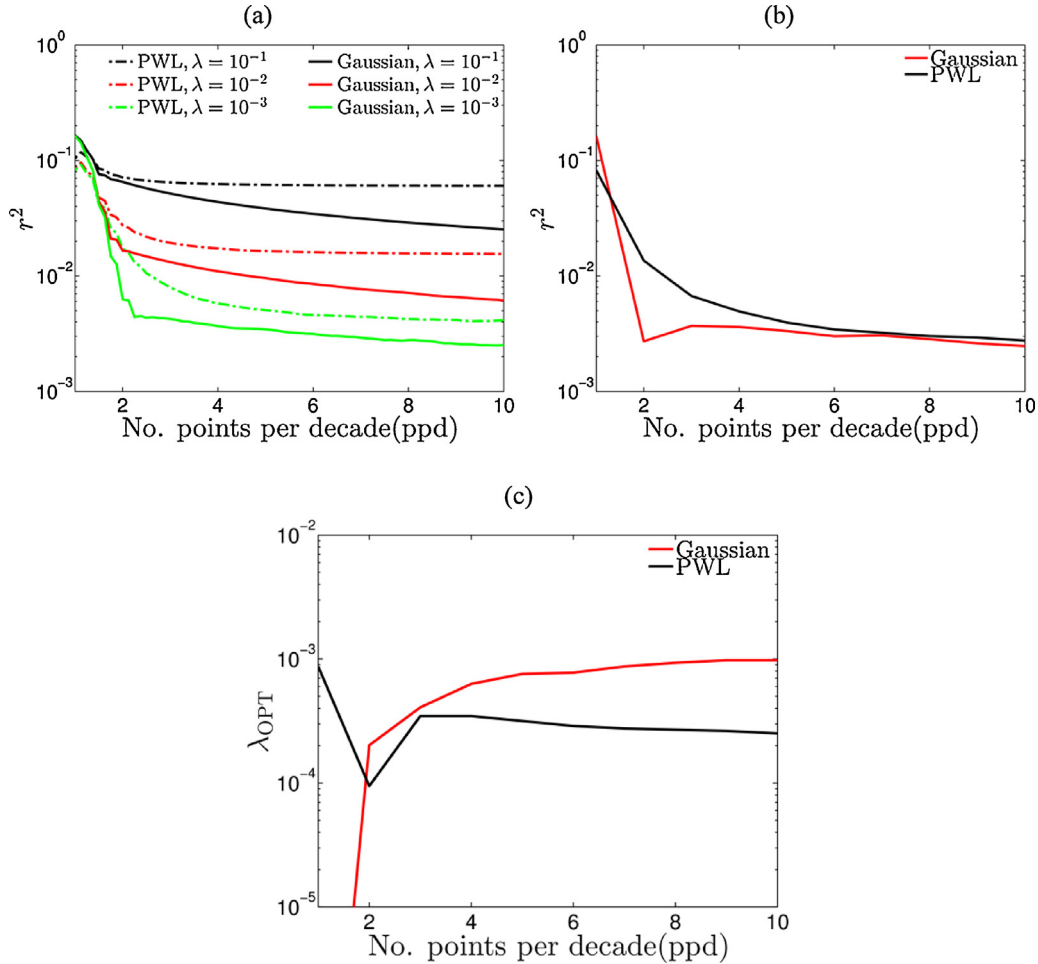

Fig. 8. The squared residual of the deconvolved DRT of the ZARC model with respect to the number of collocation points per decade at error free situation. $\lambda = 10^{-11}$ is chosen for regularization.

As shown in Fig. 6 panel a and b, the bias and variance with respect to τ, i.e., (20) and (21), of both PWL and Gaussian are comparable over the data collection range. The bias is highest at $\tau = 0.01$ s, which corresponds to the DRT peak. The bias notably increases at the edges of the data collection range. Therefore, the peak and the edges of the DRT are more susceptible to the bias in approximation. In addition, the variance is the greatest at $\tau \approx 0.1$ s, and in general it increases with τ. This is because the error structure considered, see (14), depends on $|Z(f)|$, whose magnitude increases with decreasing f (or increasing τ). Similar as the bias, the variance increases near the edges of the data collection range indicating that the extremities of the DRT are more susceptible to increased variance.

When the width of the collocation points range is halved, the average squared residuals of the DRTs computed by both methods increase, implying that the discrepancy between the computed results and the exact solution is greater, see Table 2. Reducing the range has a greater effect on the DRT estimated with the PWL discretization. If the range of data collection is reduced by half, the squared residuals of the computed DRT using PWL discretization increase by about 50 %, whereas the squared residuals of the RBFs increase only by 16-19 %. The average DRT profile when the data collection range is reduced by half is shown in Fig. 7. As shown in Fig. 7a, the Gaussian discretization allows the approximating the

Fig. 9. The average squared residual of the deconvolved DRT of the ZARC model at error level of 0.1%, panel (a), the average squared residual at optimal λ, panel (b), and the optimal λ, panel (c), with respect to the number of collocation points per decade.

convergence of $\gamma(\tau)$ as $\tau \to 0$ and $\tau \to +\infty$. Also a better estimation at the edge of data collection range is observed as compared to the PWL case, Fig. 7c. This illustrates the slight improvement in the estimation of DRT with Gaussian discretization.

If we plot the bias and variance results against τ, we observe that the peak of the bias is found at $\tau = 0.01$ s, and is increased at the two edge of the data collection range, i.e., when τ equals to 10^{-4} and 1 s, as illustrated in Fig. 6c. The PWL-based DRT leads to a larger bias over the entire τ range. On the other hand, the variances for the two type of discretizations, as shown in Fig. 6d, remain at the same level over the entire timescales with a general increasing trend between 10^{-4} and 1 s, which is also illustrated by the confidence interval in Fig. 7a and b. We note that both the variance and bias of the Gaussian-based DRT decrease quickly as $\tau \to 0$ and $\tau \to +\infty$ because Gaussian discretization allows the estimation of the DRT profile outside the data collection range, such that $\hat{\gamma}_k(\tau) \to 0$ as $\tau \to 0$ and $\tau \to +\infty$, as shown in Fig. 7a. When $\gamma_{\text{exact}}(\tau) \to 0$ as $\tau \to 0$ and $\tau \to +\infty$, the bias of the Gaussian-based DRT then decreases eventually in accordance with $\gamma_{\text{exact}}(\tau)$. Also, as $\tau \to 0$ and $\tau \to +\infty$, $\hat{\gamma}_k(\tau) \to 0$ and hence, $\frac{1}{K}\sum_{k=1}^{K}\hat{\gamma}_k(\tau) \to 0$, the variance of the Gaussian-based DRT thus reduces quickly by expression (21).

Moreover, when the collocation point density is lower by half, the squared residuals increase by 30-40 % for all types of discretization, see Table 2. In other word, the squared residuals of the RBF-based DRT do not reduce in a faster rate as compared with that of the PWL-

based DRT with respect to the collocation point density. This seems to contradict with the spectral convergence as mentioned in the literature [45,46]. To investigate the convergence of the discretization methods, we deconvolve the DRT from the error free impedance data of the ZARC model (with the parameters being the same as previously) with respect to the variation of collocation point density. We then compare the squared residual, as defined by (15), of the Gaussian-based DRT result with that of the PWL-based DRT result at various collocation point density. As shown in Fig. 8, the squared residual of the Gaussian-based DRT decays with a much faster rate than that of PWL-based DRT, especially when the collocation point density is coarse.

To further study the effect of error level on the convergence rate, we add 0.1 % random error to the ZARC model and investigate the variation of squared residual with respect to collocation point density. For $\lambda = 10^{-1}$ to 10^{-3}, Gaussian discretization will lead to faster convergence rate as compared with the PWL discretization as shown in Fig. 9a. This is true, however, only when λ are not optimized. As shown in Fig. 9b, if we optimize λ with respect to the collocation point density, it is shown that the Gaussian discretization converge faster than the PWL discretization only when the collocation point density is small. At collocation point density of 3 ppd or above, the convergence rate of the two discretization methods are comparable, which is in agreement with the results in Table 2. Thus, the convergence rate of RBF based DRT is faster than that of the PWL-based DRT only at the error free situation, when the optimization of λ is not necessary.
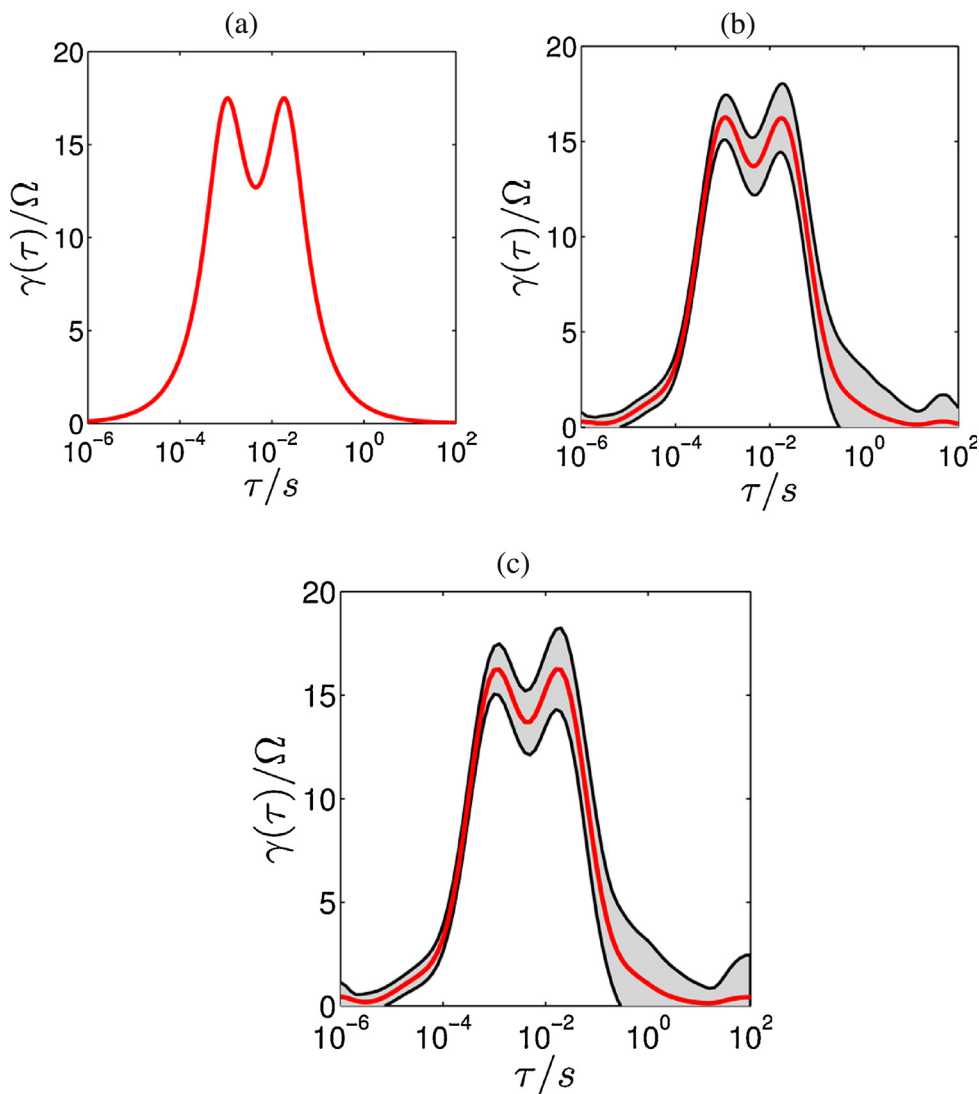
Fig. 10. The exact DRT result of the double ZARC element case, panel (a), the average computed DRT with normal data range and 10 ppd data collection density using Gaussian discretization, panel (b), and using PWL discretization, panel (c), at optimal λ. The grey band in panel (b) and (c) shows the 3σ confidence interval of the result.

Table 3
The minimum residual, optimal λ and predicted optimal λ from cross validation test for the double ZARC model with different discretization functions and data collection scenarios.

|	Normal range 10 ppd			Normal range 5 ppd			Half width range 10 ppd		
	r^2_{tot}	λ_{OPT}	λ_{CV}	r^2_{tot}	λ_{OPT}	λ_{CV}	r^2_{tot}	λ_{OPT}	λ_{CV}
Piecewise linear	1.37E-02	2.34E-03	3.02E-03	1.95E-02	3.47E-03	4.79E-03	5.19E-02	3.72E-03	1.38E-03
Gaussian	1.31E-02	1.10E-02	1.05E-02	1.83E-02	7.94E-03	1.05E-02	2.95E-02	1.02E-02	3.80E-03
C2 Matérn	1.25E-02	9.77E-03	1.10E-02	1.79E-02	6.46E-03	1.17E-02	2.83E-02	1.02E-02	7.08E-03
C4 Matérn	1.16E-02	1.02E-03	1.15E-03	1.74E-02	8.32E-04	9.77E-04	2.86E-02	1.12E-03	5.75E-04
C6 Matérn	1.27E-02	4.68E-05	5.25E-05	1.81E-02	3.39E-05	5.89E-05	2.91E-02	4.68E-05	2.95E-05

3.1.2. Series ZARC Model

In order to demonstrate that the above discussion can also be applied to systems with overlapping relaxation characteristics, we considered the case when two ZARCs are placed in series. This equivalent circuit is also commonly used in practical analysis of EIS data in the fuel cell community [62,63]. The impedance response of this circuit is:

$$Z(f) = R_\infty + \frac{R_{ct}}{1 + (i2\pi f \tau_0)^\phi} + \frac{R'_{ct}}{1 + (i2\pi f \tau'_0)^{\phi'}} \tag{24}$$

Although, in experiment, it is more common to have two CPE elements such that $R'_{ct} \neq R_{ct}$ and $\phi' \neq \phi$, in order to streamline our study, and
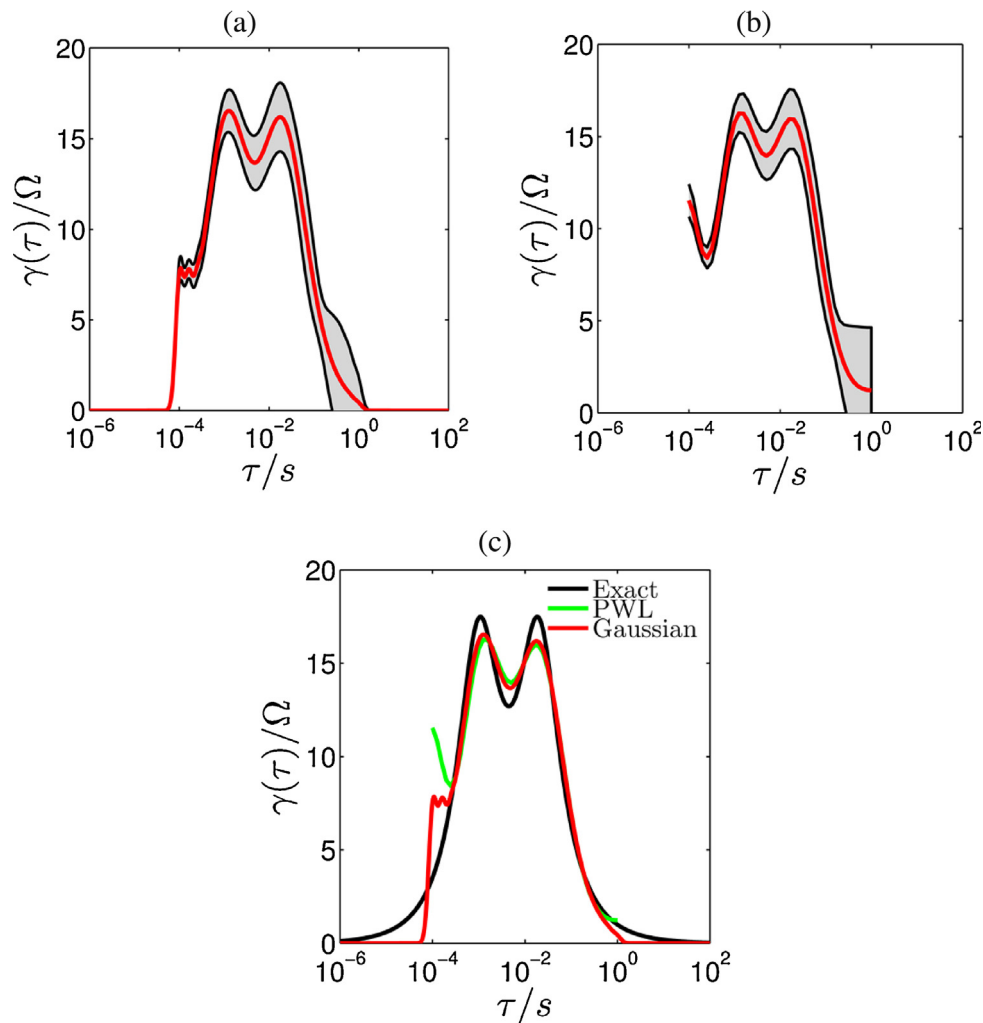
Fig. 11. The average DRT value and the confidence region for Gaussian discretization, panel (a) and PWL discretization, panel (b) for the series ZARC case with half data collection width. Panel (c) shows the comparison of the average values with the exact solution.

avoid extra degree of freedom on R'_{ct} or ϕ', here we just consider the case where $R'_{ct} = R_{ct}$ and $\phi' = \phi$ (equal to the parameter values in previous section) but with $\tau_0 = 0.02$ s and $\tau'_0 = 0.001$ s. The corresponding DRT for the series ZARC model is:

$$\gamma(\tau) = \frac{R_{ct}}{2\pi}\sin((1-\phi)\pi)\left(\frac{1}{\cosh\left(\phi\ln\left(\frac{\tau}{\tau_0}\right)\right) - \cos((1-\phi)\pi)}\right.$$

$$\left. + \frac{1}{\cosh\left(\phi\ln\left(\frac{\tau}{\tau'_0}\right)\right) - \cos((1-\phi)\pi)}\right)$$

The exact solution of the given double ZARC model is shown in Fig. 10a. The average computed DRT result using PWL discretization and RBFs discretization for the normal data collection range and data point density of 10 ppd are shown in Fig. 10b and c, respectively. The corresponding squared residuals for each data collection scenario are tabulated in Table 3. For the normal data collection range and a data density of 10 ppd, as shown in Fig. 10, the DRTs estimated using both discretization methods are consistent with the exact solution. This is true despite differences in magnitude of the peaks. Particularly, the results successfully identify the two peaks and their relaxation characteristics.

Similar to the trend of the single ZARC case, reducing the collocation points density leads to an increase in average squared residual for all types of discretization by 40-50 %. On the other hand, when the data collection range is reduced from 10^{-2} Hz $< f_m < 10^6$ Hz to 10^0 Hz $< f_m < 10^4$ Hz there is apparent discrepancy between the computed DRT and the exact solution as indicated by the average squared residual. As shown in Table 3, the average squared residual of PWL-based DRT is five times greater than the squared residual obtained from the regular data collection situation. In contrast, the average squared residual for all RBF-based discretization is only 60 % of the PWL approximation. The average DRT result for the two types of discretization is shown in Fig. 11. If we compare the estimated DRT profile by the two methods with that of the exact DRT, as shown in Fig. 11c, the Gaussian discretization allows the convergence of the result to zero as to $\tau \to 0$ and $\tau \to +\infty$, whereas the DRT result for the PWL discretization point upward at $\tau = 10^{-4}$ s. This leads to smaller bias for the Gaussian discretization and we may conclude that RBF-based DRT performs better than that of PWL when the data collection range is reduced by half.

3.1.3. Havriliak-Negami Model

The application of Havriliak-Negami model [64,65] is common in the field of corrosion science [66,67]. This model was chosen for
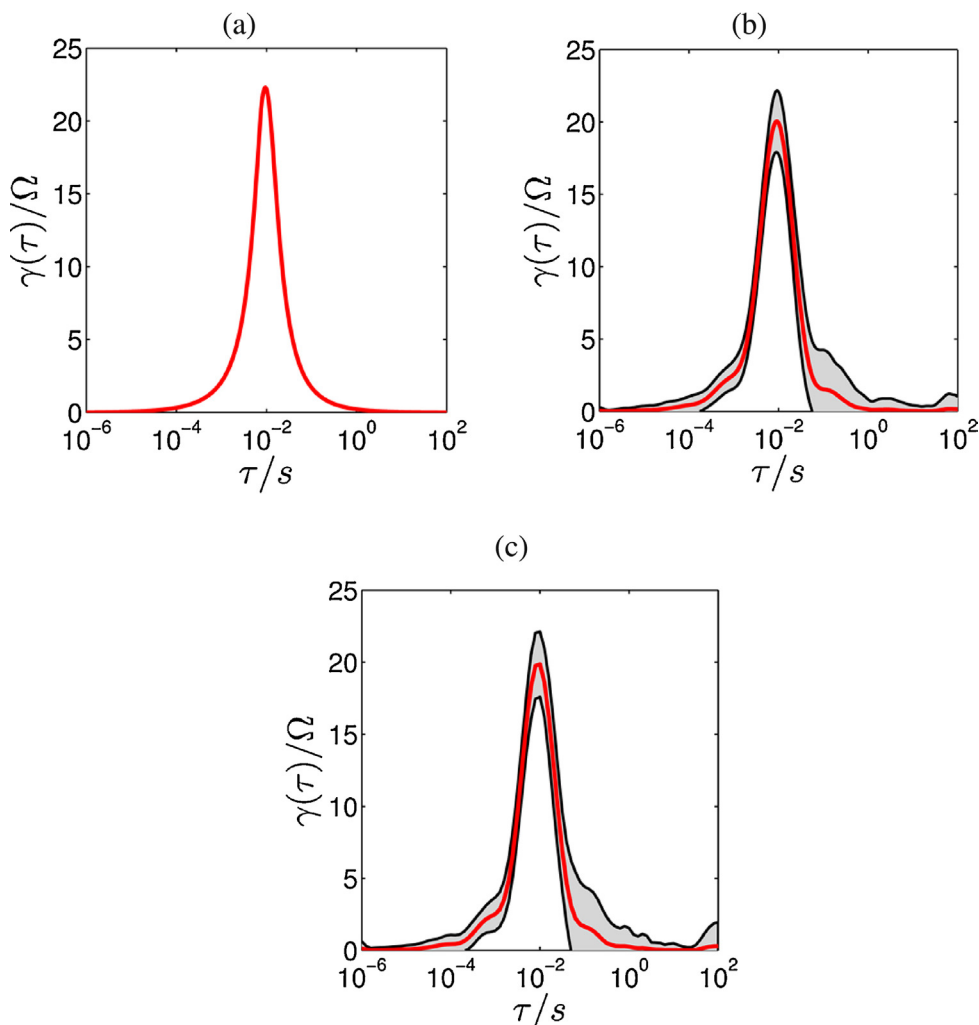
Fig. 12. The exact DRT result of the Havriliak-Negami case, panel (a), the average computed DRT with normal data range and 10 ppd data collection density using Gaussian discretization, panel (b), and using PWL discretization, panel (c), at optimal λ. The grey band in panel (b) and (c) shows the 3σ confidence interval of the result.

Table 4
The minimum residual, optimal λ and predicted optimal λ from cross validation test for the Havriliak-Negami model with different discretization functions and data collection scenarios.

	Normal range 10 ppd			Normal range 5 ppd			Half width range 10 ppd		
	r^2_{tot}	λ_{OPT}	λ_{CV}	r^2_{tot}	λ_{OPT}	λ_{CV}	r^2_{tot}	λ_{OPT}	λ_{CV}
Piecewise linear	5.19E-02	2.14E-04	3.98E-04	5.99E-02	3.31E-04	5.50E-04	9.10E-02	2.88E-04	1.15E-03
Gaussian	5.05E-02	8.71E-04	1.66E-03	5.64E-02	6.31E-04	1.66E-03	5.60E-02	1.26E-03	3.98E-03
C2 Matérn	4.84E-02	7.94E-04	2.00E-03	5.00E-02	4.57E-04	1.20E-03	5.59E-02	1.38E-03	3.47E-03
C4 Matérn	5.15E-02	1.05E-04	3.16E-04	5.31E-02	6.03E-05	1.91E-04	5.54E-02	1.38E-04	4.79E-04
C6 Matérn	5.13E-02	4.37E-06	8.91E-06	5.69E-02	2.51E-06	7.94E-06	5.72E-02	6.31E-06	1.91E-05

our study in order to further confirm that RBFs improve the DRT approximation quality. The impedance response of Havriliak-Negami model is given by:
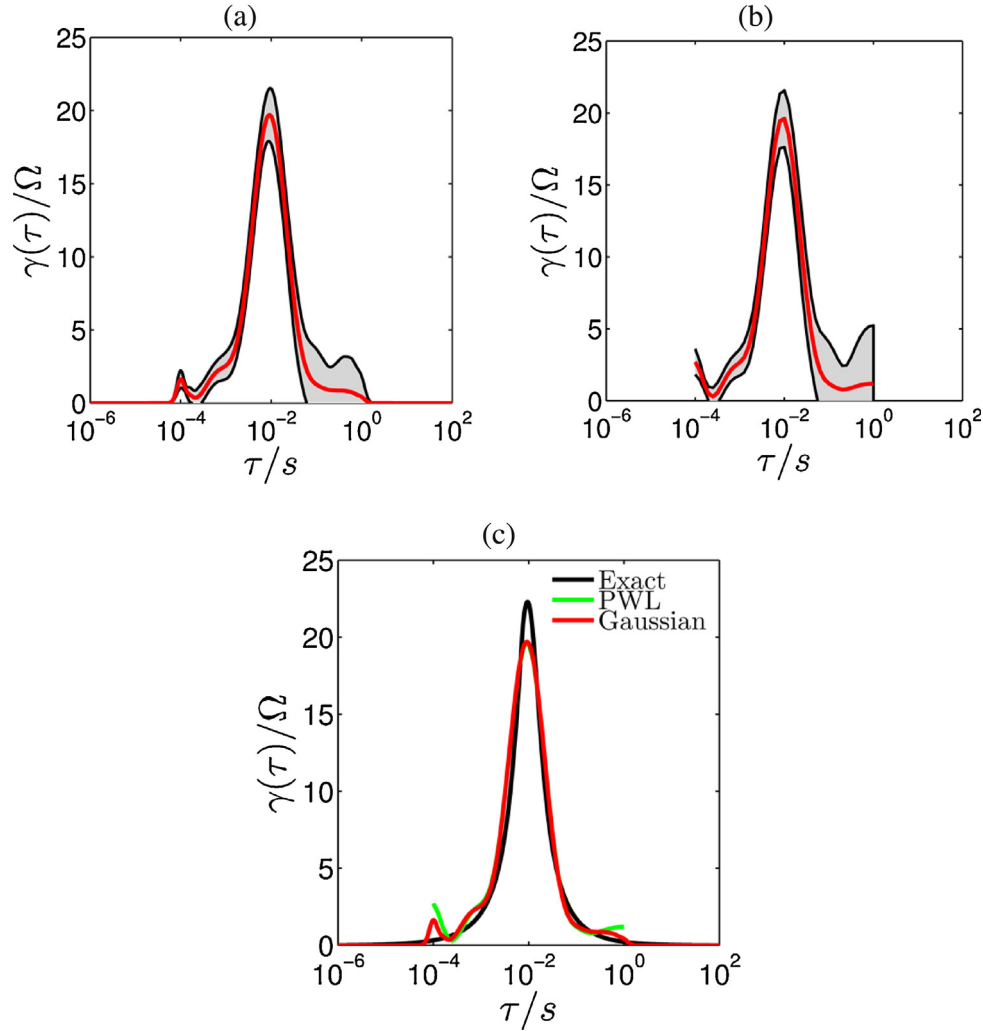
$$Z(f) = R_\infty + \frac{R_{ct}}{\left(1 + (i2\pi f \tau_0)^\phi\right)^\psi} \tag{26}$$

where $R_\infty = 10\ \Omega$, $R_{ct} = 50\ \Omega$, $\tau_0 = 0.01$ s, $\phi = 0.8$ and $\psi = 0.9$.[9] The corresponding $\gamma(\tau)$ is given by [68]

$$\gamma(\tau) = \frac{R_{ct}}{\pi} \frac{\left(\frac{\tau}{\tau_0}\right)^{\phi\psi} \sin(\psi\theta)}{\left(\left(\frac{\tau}{\tau_0}\right)^{2\phi} + 2\left(\frac{\tau}{\tau_0}\right)^\phi \cos(\pi\phi) + 1\right)^{\frac{\psi}{2}}} \tag{27}$$

where $\theta = \arctan\left|\frac{\sin(\pi\phi)}{\left(\frac{\tau}{\tau_0}\right)^\phi + \cos(\pi\phi)}\right|$. The average DRTs, for the normal

---

[9] When $\phi = 1$ and $\psi = 0.5$, one may obtain the Gerischer impedance [64,65].

Fig. 13. The average DRT value and the confidence region for Gaussian discretization, panel (a) and PWL discretization, panel (b) for the Havriliak-Negami case with half data collection width. Panel (c) shows the comparison of the average values with the exact solution.

data collection scenario, computed using the two types of discretizations are plotted and compared with the exact solution in Fig. 12. The squared residual, λ_{OPT} and λ_{CV} of the as-computed DRT in the three scenarios are reported in Table 4. The squared residual of the RBF-based DRT and that of PWL-based DRT are around the same level for the first two data collection scenarios, i.e., for the regular data collection range with 10 ppd and 5 ppd. Such trend is similar to the previous two models. When the data collection range is reduced by half, the average squared residual for the PWL-based DRT is 60 % higher than that of the RBF-based DRT. The corresponding average DRT result is shown in Fig. 13, which have shown similar trend as previous case, particularly, the RBF discretization allows improvement in approximation at the edge of data collection range. The result further confirms that the RBFs discretization allows improvement in the DRT results, only when the data collection range is limited.

3.1.4. Commentary

The improvement of the DRT obtained with RBFs when the data collection range is reduced, can be explained by the different nature of RBFs discretization and PWL discretization. For the PWL case, each one of the "tent" functions applied for discretizing $\gamma(\tau)$ has a peak at the collocation point $\ln\tau_m$ and decrease linearly to zero towards

$\ln\tau_{m-1}$ and $\ln\tau_{m+1}$. $\gamma(\tau)$ is set to zero for $\ln\tau < \ln\tau_1$ and $\ln\tau > \ln\tau_M$. Thus, the fitting of $\gamma(\tau)$ disregards what happens outside this range In contrast, the RBFs chosen in this study with the given shape parameter condition have a domain that extends to $(-\infty, \infty)$. They converge to zero when $\ln\tau \to \pm\infty$. This allows the consideration of the asymptotic conditions of $\gamma(\tau)$ during fitting. In fact, if the frequency range is being truncated, we convert the fitting model:

$$Z_{DRT} = R_\infty + \int_{-\infty}^{\infty} \frac{\gamma(\ln\tau)}{1 + i2\pi f\tau} d\ln\tau$$
$$\approx R_\infty + \int_{\ln\tau_0}^{\ln\tau_M} \frac{\sum_{m=1}^{M} x_m \phi_m(\ln\tau)}{1 + i2\pi f\tau} d\ln\tau \tag{28}$$

where $[\ln\tau_0, \ln\tau_M]$ define the range of data collection. Application of the RBF basis may impact the DRT deconvolution problem by extending the range of integration, which leads to a better approximation of the truncated integral [69]. This, in turn, reduces the squared residual within the measurement range as compared with PWL approach when the frequency range is truncated (see the bias against τ plot in Fig. 6).

In practice, restriction of the data collection frame may occur, especially when collecting the impedance data at extremely low frequencies (slow relaxations). For complex electrochemical systems such as the batteries, the dynamic nature of the sample may lead to

changes in the properties after a long EIS measurement [70]. This will imply intrinsic experimental inaccuracies. In addition, in advanced EIS techniques, e.g., the atomic force microscopy based impedance spectroscopy, the frequency range cannot be too large, since the latter can affect the space resolution [71]. Nonetheless, considering the low frequency responses also implies that additional time is needed for conducting an experiment. This is particularly unfavorable when large scale data acquisitions are used [1]. Therefore, the restrictions of data collection range will affect the quality of the estimated DRT. With the application of suitably tuned RBFs, this negative effect can be mitigated.

3.2. Application to a Lithium Ion Battery Experiment

To investigate the practical utility of the RBF-based DRT, we have studied the impedance response of a commercial lithium ion battery (LiCoO$_2$ Ansmann 18650) at the states of charge (SOC) 25 %. In fact, the SOC is a key parameter for management of LIBs [72] and previous studies have shown that the DRT of a LIB is connected to the SOC [29,73,74]. The data were acquired at room temperature for frequencies between 600 Hz and 5 mHz with 10 ppd. The minimum frequency, 5 mHz, was chosen because of the experimental time limitations. In order to reduce the experimental bias and to allow better statistics, we have repeated the impedance tests 10 times. Furthermore, we applied non-parametric bootstrap to the EIS data

[75]: we have created 1000 synthetic impedance responses, each composed by randomly selecting an impedance response at each frequency, among the 10 measured values. Moreover, as the exact DRT, and hence, λ_{OPT} is not known, we arbitrarily select $\lambda = 1 \times 10^{-2}$ for both the PWL and Gaussian based DRT.

The computed average DRT results for a 25 % SOC is shown in Fig. 14, with its 3σ confidence band. The computed results show that the PWL and Gaussian based DRT are in reasonable agreement. Both methods are able to identify the major peaks at the corresponding relaxation time. There are, however, differences in the computed DRT results near the edge of the data collection range, i.e. $\tau = 1.7 \times 10^{-3}$ s and $\tau = 200$ s, corresponding to $f = 600$ Hz and 5 m Hz respectively. For the RBF-based regularization, the highest relaxation time peak locates at $\tau = 50$ s and the lowest relaxation time peak locates at $\tau = 1.9 \times 10^{-3}$ s. On the other hand, for PWL-based regularization the highest and lowest relaxation time peaks are identified at exactly the edges of the data collection range respectively. Since in principle RBF approximation, the regression has less bias with respect to the exact DRT. Even though we do not know whether there are additional peaks outside the range or the underlying assumption of decaying DRT is valid, we expect the approximation quality to increase due to RBF's ability of preconditioning the truncated integral in the fitting model.

3.3. Software Release

The MATLAB code developed as part of this work is now released as a freely available MATLAB GUI, named, DRTtools [76]. The GUI interfaces the DRT computation via PWL and RBFs, including Gaussian, C2, C4, C6 Matérn RBFs, and beyond. The users can choose the regularization parameter λ, the μ values, and the portion of data (real, imaginary or both) that will be used for the DRT estimation. In turn, the deconvolved DRT is presented in a figure panel and can be saved as MATLAB figure, txt, or csv file. Details of the GUI features are shown in the user manual.

4. Conclusions

In this article, we have shown the importance of choosing a suitable discretization basis for estimation of DRT with regularization regression. We thus proposed a novel regularization technique for estimating DRT based on RBFs discretization. The RBFs discretization is considered because it can, in principle, achieve fast convergence with fewer sampling points, while implementation is less complex, compared with other pseudo-spectral methods. The performance of the RBF-based regularization is compared with that of a PWL-based regularization by synthetic experiments of three EIS models, which have shown an improvement in the estimation of the DRT only when the data collection range is limited. Such improvement is a result of the fact that each RBF discretization function being chosen in this study has a domain of $(-\infty, \infty)$. For this reason, the DRT approximation is estimated outside the measured frequency range, with the assumption that the underlying DRT decays to zero quickly as the logarithm of the timescale goes to infinity. It also extends the range of the original integral problem, which, in turn, leads to the reduction in average squared residual. In addition, by calculating the squared residual with various number of collocation points, it is shown that the RBF-based regularization can lead to faster convergence rate as compared with that of the PWL-based regularization only at error free situation.

We further enrich our discussion by interpreting the EIS data of a LIB at 25% SOC. Both RBF and PWL discretization have successfully identified the major peaks of the DRT but truncation
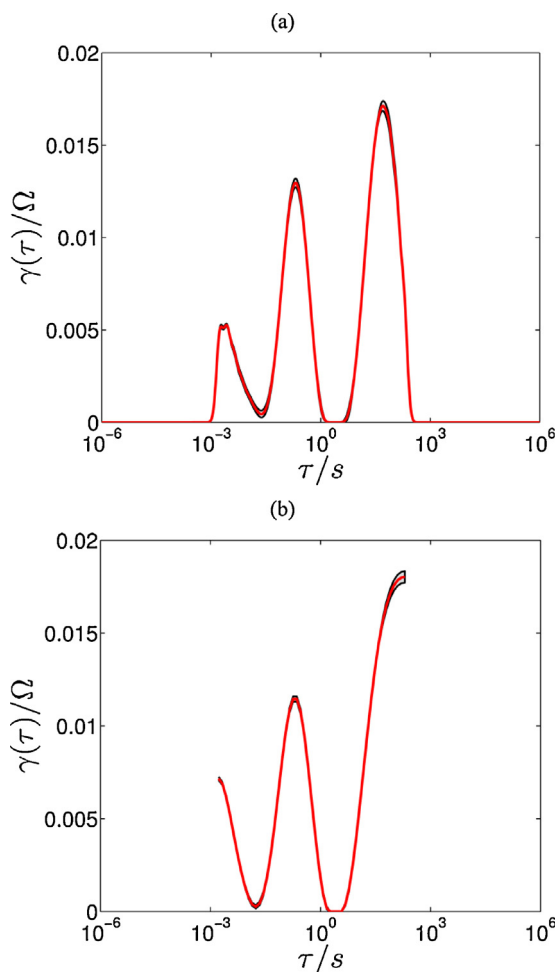
Fig. 14. The DRT results computed with the imaginary part of the experiment data for the LIBs at 25 % state of charge using Gaussian discretization, panel (a), and PWL discretization, panel (b). Regularizations are done with $\lambda = 10^{-2}$. The grey region indicates the 3σ confidence interval.

of peak occurred for the PWL-based DRT results. Based on our discussion on the synthetic experiments, we conclude that RBFs allow a reasonable prediction of the converging behavior of the exact DRT if the underlying DRT goes to zero sufficiently fast for $\ln\tau \to \pm\infty$. Nonetheless, we need to highlight that other potential advantages of RBFs for DRT should further be explored. For example, the shape factor, i.e. μ in (7) and Table 1, may be investigated as an additional smoothing effect to the regularized regression. In addition, as RBFs do not have restrictions on the collocation points distribution, they can, in principle, be applied for approximating the DRT from highly scattered data, data with missing data points, censored data, or non-uniform data sets [77]. Furthermore, the application of RBFs basis could be explored further with proper enrichment in order to handle the discontinuities in the exact DRT profile (e.g. DRT of fractal elements) [78].

Acknowledgments

Appendix A.

The DRT function $\gamma(\ln\tau)$ can be approximate by a certain discretization function $\phi_\mu(|\ln\tau - \ln\tau_m|)$, at collocation points, $\tau_1, \tau_2, \ldots \tau_M$.

$$\gamma(\ln\tau) = \sum_{m=1}^{M} x_m \phi_\mu(|\ln\tau - \ln\tau_m|) \tag{29}$$

One should note that (29) is identical to (7). In this work, $\phi_\mu(|\ln\tau - \ln\tau_m|)$ indicates an RBF. The impedance response as obtained from the DRT result using the relation (2).

$$
\begin{aligned}
Z_{\mathrm{DRT}}(f) &= R_\infty + \int_{-\infty}^{\infty} \frac{\gamma(\ln\tau)}{1 + \mathrm{i}2\pi f\tau} \mathrm{d}\ln\tau \\
&= R_\infty + \sum_{m=1}^{M} x_m \int_{-\infty}^{\infty} \frac{\phi_\mu(|\ln\tau - \tau_m|)}{1 + \mathrm{i}2\pi f\tau} \mathrm{d}\ln\tau \\
&= R_\infty + \sum_{m=1}^{M} x_m \left(\int_{-\infty}^{\infty} \frac{1}{1 + (2\pi f\tau)^2} \phi_\mu(|\ln\tau - \ln\tau_m|) \mathrm{d}\ln\tau \right. \\
&\quad \left. - i \int_{-\infty}^{\infty} \frac{2\pi f\tau}{1 + (2\pi f\tau)^2} \phi_\mu(|\ln\tau - \ln\tau_m|) \mathrm{d}\ln\tau \right)
\end{aligned}
\tag{30}
$$

We can express (20) in matrix notation by writing

$$Z_{\mathrm{DRT}}(f_n) = R_\infty + \sum_{m=1}^{M} \left[(\boldsymbol{A}')_{nm} x_m + i(\boldsymbol{A}'')_{nm} x_m \right] \tag{31}$$

which is identical to (9). $\boldsymbol{A}'$ and $\boldsymbol{A}''$ matrices are defined as

$$(\boldsymbol{A}')_{nm} = \int_{-\infty}^{\infty} \frac{1}{1 + 4\pi^2 e^{2(y + \ln f_n - \ln f_m)}} \phi_\mu(|y|) \, dy \tag{32}$$

and,

$$(\boldsymbol{A}'')_{nm} = \int_{-\infty}^{\infty} \frac{2\pi e^{y + \ln f_n - \ln f_m}}{1 + 4\pi^2 e^{2(y + \ln f_n - \ln f_m)}} \phi_\mu(|y|) dy \tag{33}$$

where we take $y = \ln\tau - \ln\tau_n$. One should note that if the frequencies are logarithmically equispaced, i.e., $(\ln f_n - \ln f_m) \propto (n - m)$, then $\boldsymbol{A}'$ and $\boldsymbol{A}''$ are diagonal-constant

matrices, or Toeplitz matrices. One may then apply the definition of $\boldsymbol{A}'$ and $\boldsymbol{A}''$ for the sum of squares in (11).

In addition, to stabilize the DRT result, a penalty term is added in (11), which is the square of the norm of the first derivative of the DRT function

$$\frac{d\gamma(\ln\tau)^2}{d\ln\tau} = \boldsymbol{x}^T \boldsymbol{M}\boldsymbol{x} = \sum_{m=1}^{M}\sum_{l=1}^{M} x_l x_m (\boldsymbol{M})_{lm} \tag{34}$$

Since,

$$\frac{d\gamma(\ln\tau)^2}{d\ln\tau} = \int_{-\infty}^{\infty} \left(\frac{d\gamma(\ln\tau)}{d\ln\tau} \right)^2 d\ln\tau \tag{35}$$

by applying relation (7) we have

$$\frac{d\gamma(\ln\tau)}{d\ln\tau} = \sum_{m=1}^{M} x_m \frac{d\phi_\mu(|\ln\tau - \ln\tau_m|)}{d\ln\tau} \tag{36}$$

Thus

$$\left(\frac{d\gamma(\ln\tau)}{d\ln\tau} \right)^2 = \sum_{l=1}^{M}\sum_{m=1}^{M} x_l x_m \frac{d\phi_\mu(|\ln\tau - \ln\tau_l|) d\phi_\mu(|\ln\tau - \ln\tau_m|)}{d\ln\tau \quad d\ln\tau} \tag{37}$$

By integrating (27) and comparing the coefficient of the $x_l x_m$ term in (24), we can derive the expression for the matrix $\boldsymbol{M}$

$$(\boldsymbol{M})_{lm} = \int_{-\infty}^{\infty} \frac{d\phi_\mu(|\ln\tau - \ln\tau_l|) d\phi_\mu(|\ln\tau - \ln\tau_m|)}{d\ln\tau \quad d\ln\tau} d\ln\tau \tag{38}$$

One notes that if the frequencies are equispaced in logarithm scale then $\boldsymbol{M}$ is also a Toeplitz matrix.

In addition, the matrix $\boldsymbol{\Omega}'$ and $\boldsymbol{\Omega}''$ in (10) are expressed as

$$\left(\boldsymbol{\Omega}' \right)_{n,m} = \delta_{n,m} \sqrt{w''_{n,m}} \tag{39}$$

$$\left(\boldsymbol{\Omega}'' \right)_{n,m} = \delta_{n,m} \sqrt{w''_{n,m}} \tag{40}$$

where $n = 1, \ldots, N$ and $m = 1, \ldots, M$

References

[1] J.R. Macdonald, E. Barsoukov, Impedance spectroscopy: Theory, experiment, and applications, History 1 (2005) 8.

[2] J.P. Schmidt, T. Chrobak, M. Ender, J. Illig, D. Klotz, E. Ivers-Tiffée, Studies on LiFePO$_4$ as cathode material using impedance spectroscopy, Journal of Power Sources 196 (2011) 5342–5348.

[3] T.E. Springer, T.A. Zawodzinski, M.S. Wilson, S. Gottesfield, Characterization of polymer electrolyte fuel cells using AC impedance spectroscopy, Journal of The Electrochemical Society 143 (1996) 587–599.

[4] Z. He, F. Mansfeld, Exploring the use of electrochemical impedance spectroscopy (EIS) in microbial fuel cell studies, Energy & Environmental Science 2 (2009) 215–219.

[5] A.C. Ciubotariu, L. Benea, M. Lakatos-Varsanyi, V. Dragan, Electrochemical impedance spectroscopy and corrosion behaviour of Al$_2$O$_3$–Ni nano composite coatings, Electrochimica Acta 53 (2008) 4557–4563.

[6] A. Nishikata, Y. Ichihara, T. Tsuru, An application of electrochemical impedance spectroscopy to atmospheric corrosion study, Corrosion Science 37 (1995) 897–911.

[7] F. Fabregat-Santiago, J. Bisquert, G. Garcia-Belmonte, G. Boschloo, A. Hagfeldt, Influence of electrolyte in transport and recombination in dye-sensitized solar cells studied by impedance spectroscopy, Solar Energy Materials and Solar Cells 87 (2005) 117–131.

[8] Q. Wang, J.-E. Moser, M. Grätzel, Electrochemical impedance spectroscopic analysis of dye-sensitized solar cells, The Journal of Physical Chemistry B 109 (2005) 14945–14953.

[9] U.G. Kyle, I. Bosaeus, A.D. De Lorenzo, P. Deurenberg, M. Elia, J.M. Gómez, B.L. Heitmann, L. Kent-Smith, J.-C. Melchior, M. Pirlich, H. Scharfetter, A.M.W.J. Schols, C. Pichard, Bioelectrical impedance analysis—part I: Review of principles and methods, Clinical Nutrition 23 (2004) 1226–1243.

[10] M. Van Loan, P., Withers, J., Matthie, P., Mayclin, Use of bioimpedance spectroscopy to determine extracellular fluid, intracellular fluid, total body water, and fat-free mass, in: K. Ellis, J. Eastman (Eds.) Human Body Composition, Springer US, 1993, pp. 67-70.

[11] E. Katz, I. Willner, Probing biomolecular interactions at conductive and semiconductive surfaces by impedance spectroscopy: Routes to impedimetric immunosensors, DNA-sensors, and enzyme biosensors, Electroanalysis 15 (2003) 913–947.

[12] W. Franks, I. Schenker, P. Schmutz, A. Hierlemann, Impedance characterization and modeling of electrodes for biomedical applications, Biomedical Engineering, IEEE Transactions on 52 (2005) 1295–1302.

[13] R. Go, R. Bashir, A. Sarikaya, M. Ladisch, J. Sturgis, J. Robinson, T. Geng, A. Bhunia, H. Apple, S. Wereley, Microfluidic biochip for impedance spectroscopy of biological species, Biomedical Microdevices 3 (2001) 201–209.

[14] L. Han, N. Koide, Y. Chiba, T. Mitate, Modeling of an equivalent circuit for dye-sensitized solar cells, Applied Physics Letters 84 (2004) 2433–2435.

[15] C.H. Chen, J. Liu, K. Amine, Symmetric cell approach and impedance spectroscopy of high power lithium-ion batteries, Journal of Power Sources 96 (2001) 321–328.

[16] J.T. Müller, P.M. Urban, W.F. Hölderich, Impedance studies on direct methanol fuel cell anodes, Journal of Power Sources 84 (1999) 157–160.

[17] M. Kissi, M. Bouklah, B. Hammouti, M. Benkaddour, Establishment of equivalent circuits from electrochemical impedance spectroscopy study of corrosion inhibition of steel by pyrazine in sulphuric acidic solution, Applied Surface Science 252 (2006) 4190–4197.

[18] J.R. Macdonald, Impedance spectroscopy: Old problems and new developments, Electrochimica Acta 35 (1990) 1483–1492.

[19] F. Dion, A. Lasia, The use of regularization methods in the deconvolution of underlying distributions in electrochemical processes, Journal of Electroanalytical Chemistry 475 (1999) 28–37.

[20] V. Sonn, A. Leonide, E. Ivers-Tiffée, Combined deconvolution and CNLS fitting approach applied on the impedance response of technical Ni/8YSZ cermet electrodes, Journal of The Electrochemical Society 155 (2008) B675–B679.

[21] A. Borenstein, S. Hershkovitz, A. Oz, S. Luski, Y. Tsur, D. Aurbach, Use of 1,10-Phenanthroline as an Additive for High-Performance Supercapacitors, The Journal of Physical Chemistry C 119 (2015) 12165–12173.

[22] A. Tesler, D. Lewin, S. Baltianski, Y. Tsur, Analyzing results of impedance spectroscopy using novel evolutionary programming techniques, Journal of Electroceramics 24 (2010) 245–260.

[23] S. Hershkovitz, S. Baltianski, Y. Tsur, Harnessing evolutionary programming for impedance spectroscopy analysis: A case study of mixed ionic-electronic conductors, Solid State Ionics 188 (2011) 104–109.

[24] S. Hershkovitz, S. Tomer, S. Baltianski, Y. Tsur, ISGP: impedance spectroscopy analysis using evolutionary programming procedure, ECS Transactions 33 (2011) 67–73.

[26] E. Tuncer, S. Gubanski, On dielectric data analysis. Using the Monte Carlo method to obtain relaxation time distribution and comparing non-linear spectral function fits, Dielectrics and Electrical Insulation, IEEE Transactions on 8 (2001) 310–320.

[27] E. Tuncer, J.R. Macdonald, Comparison of methods for estimating continuous distributions of relaxation times, Journal of Applied Physics 99 (2006) 074106.

[28] T. Hörlin, Deconvolution and maximum entropy in impedance spectroscopy of noninductive systems, Solid State Ionics 107 (1998) 241–253.

[29] J. Illig, J.P. Schmidt, M. Weiss, A. Weber, E. Ivers-Tiffée, Understanding the impedance spectrum of 18650 LiFePO$_4$-cells, Journal of Power Sources 239 (2013) 670–679.

[30] B.A. Boukamp, Fourier transform distribution function of relaxation times; application and limitations, Electrochimica Acta 154 (2015) 35–46.

[31] J. Macutkevic, J. Banys, A. Matulis, Determination of the distribution of the relaxation times from dielectric spectra, Nonlinear Analysis: Modelling and Control 9 (2004) 75–84.

[32] A. Mikonis, J. Banys, R. Grigalaitis, A. Matulis, S. Lapinskas, G. Völkel, Determination of the two dimensional distribution of the attempt relaxation times and activation energies from temperature dependence of dielectric dispersion, Central European Journal of Physics 11 (2013) 206–212.

[33] R. Renaut, R. Baker, M. Horst, C. Johnson, D. Nasir, Stability and error analysis of the polarization estimation inverse problem for microbial fuel cells, Inverse Problems 29 (2013) 045006.

[34] P.C. Hansen, Regularization tools version 4.0 for Matlab 7.3, Numerical Algorithms 46 (2007) 189–194.

[35] R. Kohn, M. Smith, D. Chan, Nonparametric regression using linear combinations of basis functions, Statistics and Computing 11 (2001) 313–322.

[36] M. Saccoccio, T.H. Wan, C. Chen, F. Ciucci, Optimal regularization in distribution of relaxation times applied to electrochemical impedance spectroscopy: Ridge and Lasso Regression methods - a theoretical and experimental study, Electrochimica Acta 147 (2014) 470–482.

[37] O. Christensen, K.L. Christensen, Approximation Theory: From Taylor Polynomials to Wavelets, Birkhauser Boston, 2012.

[38] M.D. Buhmann, Radial basis functions, Acta Numerica 2000 9 (2000) 1–38.

[39] M.D. Buhmann, Radial basis functions: Theory and implementations, Cambridge University Press Cambridge, 2003.

[40] S. Chen, C.F. Cowan, P.M. Grant, Orthogonal least squares learning algorithm for radial basis function networks, Neural Networks, IEEE Transactions on 2 (1991) 302–309.

[41] J. Wang, G. Liu, A point interpolation meshless method based on radial basis functions, International Journal for Numerical Methods in Engineering 54 (2002) 1623–1648.

[42] M.J. Orr, Introduction to radial basis function networks, Technical Report, Center for Cognitive Science, University of Edinburgh, 1996.

[43] M.T. Musavi, W. Ahmed, K.H. Chan, K.B. Faris, D.M. Hummels, On the training of radial basis function classifiers, Neural Networks 5 (1992) 595–603.

[44] J.C. Carr, R.K. Beatson, J.B. Cherrie, T.J. Mitchell, W.R. Fright, B.C. McCallum, T.R. Evans, Reconstruction and representation of 3D objects with radial basis functions, Proceedings of the 28th Annual Conference on Computer Graphics and Interactive Techniques, ACM, pp (2001) 67–76.

[45] B. Fornberg, N. Flyer, Accuracy of radial basis function interpolation and derivative approximations on 1-D infinite grids, Advances in Computational Mathematics 23 (2005) 5–20.

[46] B. Fornberg, N. Flyer, J.M. Russell, Comparisons between pseudospectral and radial basis function derivative approximations, IMA Journal of Numerical Analysis (2010) 149–172.

[47] B. Fornberg, J. Zuev, The Runge phenomenon and spatially variable shape parameters in RBF interpolation, Computers & Mathematics with Applications 54 (2007) 379–398.

[48] M.E. Orazem, P. Shukla, M.A. Membrino, Extension of the measurement model approach for deconvolution of underlying distributions for impedance measurements, Electrochimica Acta 47 (2002) 2027–2034.

[49] H. Schichlein, A.C. Müller, M. Voigts, A. Krügel, E. Ivers-Tiffée, Deconvolution of electrochemical impedance spectra for the identification of electrode reaction mechanisms in solid oxide fuel cells, Journal of Applied Electrochemistry 32 (2002) 875–882.

[50] P. Agarwal, M.E. Orazem, L.H. Garcia-Rubio, Measurement models for electrochemical impedance spectroscopy I. Demonstration of applicability, Journal of The Electrochemical Society 139 (1992) 1917–1927.

[51] J. Winterhalter, D. Ebling, D. Maier, J. Honerkamp, Analysis of admittance data: Comparison of a parametric and a nonparametric method, Journal of Computational Physics 153 (1999) 139–159.

[52] G.S. Watson, Smooth regression analysis, Sankhyā: The Indian Journal of Statistics, Series A, (1964) 359–372.

[53] L.N. Trefethen, Approximation Theory and Approximation Practice, Society for Industrial and Applied Mathematics, 2013.

[54] G. Fasshauer, RBF collocation methods and pseudospectral methods, WIT, Press, Southampton, UK, 2005, pp. 47–57.

[55] J.H. Wilkinson, The algebraic eigenvalue problem, Clarendon Press Oxford, 1965.

[56] F. Ciucci, Revisiting parameter identification in electrochemical impedance spectroscopy: Weighted least squares and optimal experimental design, Electrochimica Acta 87 (2013) 532–545.

[57] P. Agarwal, O.D. Crisalle, M.E. Orazem, L.H. Garcia-Rubio, Application of measurement models to impedance spectroscopy II. Determination of the stochastic contribution to the error structure, Journal of The Electrochemical Society 142 (1995) 4149–4158.

[58] S. Buller, M. Thele, E. Karden, R.W. De Doncker, Impedance-based non-linear dynamic battery modeling for automotive applications, Journal of Power Sources 113 (2003) 422–430.

[59] M. Ecker, J.B. Gerschler, J. Vogel, S. Käbitz, F. Hust, P. Dechent, D.U. Sauer, Development of a lifetime prediction model for lithium-ion batteries based on extended accelerated aging test data, Journal of Power Sources 215 (2012) 248–257.

[60] J.R. Dygas, Dielectric function of ionic conductors studied by impedance spectroscopy, Solid State Ionics 176 (2005) 2065–2078.

[61] R.M. Fuoss, J.G. Kirkwood, Electrical Properties of Solids. VIII. Dipole Moments in Polyvinyl Chloride-Diphenyl Systems, Journal of the American Chemical Society 63 (1941) 385–394.

[62] D. Chen, C. Chen, F. Dong, Z. Shao, F. Ciucci, Cobalt-free polycrystalline Ba$_{0.95}$La$_{0.05}$FeO$_{3-\delta}$ thin films as cathodes for intermediate-temperature solid oxide fuel cells, Journal of Power Sources 250 (2014) 188–195.

[63] W. Jung, H.L. Tuller, Investigation of Cathode Behavior of Model Thin-Film SrTi$_{1-x}$Fe$_x$O$_{3-\delta}$ (x = 0.35 and 0.5) Mixed Ionic-Electronic Conducting Electrodes, Journal of The Electrochemical Society 155 (2008) B1194–B1201.

[64] S. Havriliak, S. Negami, A complex plane representation of dielectric and mechanical relaxation processes in some polymers, Polymer 8 (1967) 161–210.

[65] B.A. Boukamp, H.J.M. Bouwmeester, Interpretation of the Gerischer impedance in solid state ionics, Solid State Ionics 157 (2003) 29–33.

[66] M. Haeri, S. Goldberg, J.L. Gilbert, The voltage-dependent electrochemical impedance spectroscopy of CoCrMo medical alloy using time-domain techniques: Generalized Cauchy–Lorentz, and KWW–Randles functions describing non-ideal interfacial behaviour, Corrosion Science 53 (2011) 582–588.

[67] M. Bojinov, V. Karastoyanov, P. Kinnunen, T. Saario, Influence of water chemistry on the corrosion mechanism of a zirconium–niobium alloy in simulated light water reactor coolant conditions, Corrosion Science 52 (2010) 54–67.

[68] F. Alvarez, A. Alegra, J. Colmenero, Relationship between the time-domain Kohlrausch-Williams-Watts and frequency-domain Havriliak-Negami relaxation functions, Physical Review B 44 (1991) 7306.

[69] J.K. Hansen, J.D. Hogue, G.K. Sander, R.A. Renaut, S.C. Popat, Non-negatively constrained least squares and parameter choice by the residual periodogram for the inversion of electrochemical impedance spectroscopy data, Journal of Computational and Applied Mathematics 278 (2015) 52–74.

[70] F. Huet, A review of impedance measurements for determination of the state-of-charge or state-of-health of secondary batteries, Journal of Power Sources 70 (1998) 59–69.

[71] R. O'Hayre, M. Lee, F.B. Prinz, Ionic and electronic impedance imaging using atomic force microscopy, Journal of Applied Physics 95 (2004) 8382–8392.

[72] S. Piller, M. Perrin, A. Jossen, Methods for state-of-charge determination and their applications, Journal of Power Sources 96 (2001) 113–120.

[73] J.P. Schmidt, P. Berg, M. Schönleber, A. Weber, E. Ivers-Tiffée, The distribution of relaxation times as basis for generalized time-domain models for Li-ion batteries, Journal of Power Sources 221 (2013) 70–77.

[74] J. Illig, T. Chrobak, D. Klotz, E. Ivers-Tiffée, Evaluation of the rate determining processes for LiFePO$_4$ as cathode material in lithium-ion-batteries, ECS Transactions 33 (2011) 3–15.

[75] A.M. Zoubir, D.R. Iskander, Bootstrap techniques for signal processing, Cambridge University Press, 2004.

[76] DRTtools and the manual, https://sites.google.com/site/drttools/.

[77] G.E. Fasshauer, J.G. Zhang, On choosing optimal shape parameters for RBF approximation, Numerical Algorithms 45 (2007) 345–368.

[78] F. Bernal, M. Kindelan, On the enriched RBF method for singular potential problems, Engineering analysis with boundary elements, 33 (2009) 1062-1073.